BRNO UNIVERSITY OF TECHNOLOGY
VYSOKÉ UČENÍ TECHNICKÉ V BRNĚ

FACULTY OF MECHANICAL ENGINEERING
FAKULTA STROJNÍHO INŽENÝRSTVÍ

INSTITUTE OF PHYSICAL ENGINEERING
ÚSTAV FYZIKÁLNÍHO INŽENÝRSTVÍ

COMPLEX ION BEAM BASED DEPTH PROFILING OF ANTICORROSIVE LAYERS
KOMPLEXNÍ IONTOVÁ ANALÝZA SLOŽENÍ ANTIKOROZNÍCH VRSTEV

MASTER'S THESIS
DIPLOMOVÁ PRÁCE

AUTHOR — **Bc. Radek Holeňák**
AUTOR PRÁCE

SUPERVISOR — **Ing. Petr Bábor, Ph.D.**
VEDOUCÍ PRÁCE

BRNO 2019

BRNO UNIVERSITY OF TECHNOLOGY
FACULTY OF MECHANICAL ENGINEERING

Specification Master's Thesis

Department:	Institute of Physical Engineering
Student:	**Bc. Radek Holeňák**
Study programme:	Applied Sciences in Engineering
Study field:	Physical Engineering and Nanotechnology
Leader:	**Ing. Petr Bábor, Ph.D.**
Academic year:	2018/19

Pursuant to Act no. 111/1998 concerning universities and the BUT study and examination rules, you have been assigned the following topic by the institute director Master's Thesis:

Complex ion beam based depth profiling of anticorrosive layers

Concise characteristic of the task:

Ion beam–based analytical techniques represent a powerful set of tools for the elemental composition analysis in the depths from several nm up to few μm. Only a combination of several ion beam–based techniques like Rutherford Backscattering Spectroscopy (RBS), Particle–Induced X–ray Emission (PIXE), Elastic Backscattering Spectroscopy (EBS) and Secondary ion mass spectrometry (SIMS) overcomes the limitations of each individual technique and provides complementary information about the sample. A combination of these techniques is often beneficial when the samples of interest contain light species in a heavy matrix, and strong gradients in concentrations may be expected. Such complex chemical compositions are, however, often the case in many of the high–tech coatings employed today in mechanically or chemically challenging environments. The aim of this diploma thesis will be to analyze such coatings by several ion beam techniques and discuss complementary information.

Goals Master's Thesis:

1. Make the PIXE method working.
2. Measure depth elemental composition of anti–corrosive alloy layers by several ion beam based techniques like RBS, PIXE and SIMS.
3. Discuss the results and compare used analytical approaches.

Recommended bibliography:

JEYNES, C., COLAUX, J. , Thin film depth profiling by ion beam analysis, Analyst 141, 2016, 5944-5985.

CARRETTE, B., L., FRIEDRICH, K., A., STIMMING, U. , Fuel Cells - Fundamentals and Applications, Fuel Cells 1, 2001, 5-39.

Deadline for submission Master's Thesis is given by the Schedule of the Academic year 2018/19

In Brno,

L. S.

prof. RNDr. Tomáš Šikola, CSc.
Director of the Institute

doc. Ing. Jaroslav Katolický, Ph.D.
FME dean

Abstract
Presented master's thesis deals with the implementation of the Particle Induced X-ray Emission method in the experimental setup with the aim to supplement the family of ion beam based techniques, i.e. Rutherford Backscattering Spectrometry, Elastic Backscattering Spectrometry and Time-of-Flight/Energy Elastic Recoil Detection Analysis. The advantage of a multi-method approach is demonstrated on the transition metal alloy films containing light species, where the self-consistent analysis yields significantly improved and accurate information about stoichiometry, depth distribution and thickness of the alloy. Secondary Ion Mass Spectrometry is employed to compare and complement the obtained results.

Abstrakt
Předložená diplomová práce se zabývá implementací metody rentgenové emisne indukované částicemi do experimentálního uspořádání za účelem doplnění rodiny metod založených na iontových technikách, tj. Rutherfordovy zpětné rozptylové spektrometrie, spektrometrie elastického zpětného rozptylu a analýzy detekce doby letu/energie elastického odrazu. Výhoda více-metodického přístupu je demonstrována na vrstvách ze slitin přechodných kovů obsahujících lehké prvky, kde samo-konzistentní analýza poskytuje výrazně zlepšené a přesné informace o stechiometrii, hloubkovém rozložení a tloušťce slitiny. Hmotnostní spektrometrie sekundárních iontů je použita pro porovnání a doplnění získaných výsledků.

Keywords
Ion Beam Analysis, composition depth profiling, PIXE

Klíčová slova
Analýza iontovým svazkem, kompozitní hloubkové profilování, PIXE

HOLEŇÁK, Radek. *Complex ion beam based depth profiling of anticorrosive layers.* Brno, 2019. 51 s. Master's thesis. Brno University of Technology. Faculty of Mechanical Engineering. Supervised by Petr BÁBOR.

I hereby declare that I have written my master's thesis on the theme of *Complex ion beam based depth profiling of anticorrosive layers* independently, under the guidance of the master's thesis supervisor, Ing. Petr Bábor, Ph.D., and using the technical literature and other sources of information which are all properly quoted in the thesis and detailed in the list of literature at the end of the thesis.

Bc. Radek Holeňák

Acknowledgement

At this point I would like to share my sincere gratitude to a number of people:

To my supervisor and friend Petr Bábor, for the four years of great collaboration, guidance, family atmosphere and trust. I will always owe you.

Big thank you belongs to Marcos Moro, my Total-IBA mentor, who took me under his wings during my stay in Sweden. Nothing of this would happen without the boss, Daniel Primetzhofer, to whom I would like to give thanks for the life changing opportunity to become a part of his research team.

I would also like to acknowledge the contribution from León Zendejas Medina from Department of Chemistry at Uppsala University, who under supervision of Ulf Jansson prepared the samples and provided them for the analysis.

I acknowledge the financial support from the European Union program for education Erasmus. Part of the work was carried out with the support of CEITEC Nano Research Infrastructure (ID LM2015041, MEYS CR, 2016–2019), CEITEC Brno University of Technology.

Last but not least: Thank you my friends Honza and Tomáš, my parents, family and Sadi, for all the support and love that were my reminders of what is truly important.

Bc. Radek Holeňák

Contents

Introduction

Entering the invisible world of matter can be only achieved in an indirect way. Modern physics discoveries allowed for the development of suitable probes to "touch" and "see" the sample of interest at the atomic and molecular level. Such probes usually originate from this microscopic world; e.g. atomic particles. Due to the interaction with the target atoms, reaction products, which might include the probing particle with modified properties, are emitted and can be detected. With the help of theoretical models, computer calculations and simulations the material nature can be discovered. Typical research questions addressed to the unknown sample are: the determination of chemical composition, atomic structure, thickness and concentration profile in the layers.

The beam of ions can serve as a very powerful probe. Ions with energies in the MeV range interact with matter in several different ways. Study of various interaction products lays the foundation for one (or more) established technique out of the Ion Beam Analysis (IBA) family. By changing the type of incident ion, the geometry of the experiment and particle energy, complementary information about the sample can be extracted. It is thus advantageous to allow for the detection of as much reaction products as possible. The most widely employed ion beam techniques are Rutherford Backscattering Spectrometry (RBS), Elastic Recoil Detection Analysis (ERDA), Elastic Backscattering Spectrometry (EBS) and Particle Induced X-ray Emission (PIXE). Typically, a combination of these ion beam-based techniques overcomes the limitations of each individual method.

Tandem laboratory, as a part of Uppsala University, Sweden, performs world-leading research with the help of ion beams. However, there was no complete experimental setup consisting of all four mentioned IBA techniques. The absence of PIXE was an establishing point for this project, which chose as its objectives to introduce the PIXE method in the experimental setup and to demonstrate its advantageous complementarity with the rest of the IBA techniques.

A combination of these techniques is often beneficial when the samples of interest contain light species in a heavy matrix. Hence, the complex system with magnetron sputtered thin layer of C/Cr/Fe/Ni was elected as a challenge for the analysis. The composition is similar to high-tech multi-elemental coatings employed today in environments where the corrosion strength is a crucial attribute of the used materials.

Aside from what is recognized as IBA techniques, another ion beam based technique called Secondary Ion Mass Spectrometry (SIMS) can contribute to the investigation on sample structure. Modern SIMS instrumentation at CEITEC, Czech Republic, was employed to compare the results obtained by IBA techniques with SIMS analysis.

It is appropriate to mention here, that part of the presented work overcame the scope of this thesis when being submitted as a scientific paper in an impacted journal. A preprint of the manuscript is included in the appendix of the thesis.

This thesis is structured as follows: Chapter 1 introduces the fundamental theoretical concepts and mechanisms of ion-target interaction that are important for the gen-

eral understanding of this work. In light of theoretical knowledge, Chapter 2 describes the IBA techniques and relevant experimental and data evaluation methods. Chapter 3 then focuses on the implementation of a PIXE station at the Tandem laboratory, Uppsala University, and reports on the accurate high-resolution depth-profiling of the chemical composition of the studied system.

1. Ion beam solid interaction

The existence of the smallest, indivisible piece of matter was theorised already in ancient Greece. Democritos called this particle as atom. The theory of various kinds of unbreakably small pieces of matter, atoms, combining to form bigger structures was accepted for millennia until the end of the 19^{th} century, when the J. J. Thompson experimentally discovered electron, the first subatomic particle. External neutrality of the atom was then explained by the presence of the negatively charged particles as raisins within the positively charged background-pudding. Rutherford's experiment at the beginning of 20^{th} century proved that most of the mass with a positive charge is located in a very small space in the centre of the atom [1]. Since then the accepted model for the structure of the atom had been that of a small positively charged nucleus surrounded by electrons in circular orbits. The radius of the atom was found to be more than 10000 times the radius of its nucleus. Each nucleus is characterized by a definite atomic number Z and mass number A. The atomic number Z is the number of positive particles (protons) and hence the number of electrons in the neutral atom; which reflects the atomic properties. The mass number gives the number of nucleons, i.e. protons and neutrons. Where the balance in number of protons and electrons is changed in the mass number the atom neutrality is disrupted and the ion is created. Ion is a charged particle that can be manipulated by application of magnetic and electric fields; and thus accelerated as a projectile.

This discovery gave birth to the ion beam techniques that are currently used for measuring the interaction of ions with targets of unknown elements to determine atomic composition.

A comprehensive understanding of the nature of particles is the key to the development of modern physics and all surface analysis techniques [2]. For the first overall understanding of the ion beam solid interaction only a basis kinematics principles are required. Such a complex problem can be described on the lowest level of the situation, where two single particles are interacting. In this chapter the fundamentals of the interaction will be stated only to the extent needed for the comprehension of this thesis.

Equations presented in following sections were derived following the book [3].

1.1. Binary collision

In the system of two isolated particles, where a single elastic collision occurs, the leading interaction principles are the conservation laws. No external force interferes with this isolated system; and thus the problem can be fully solved by applying the principles of conservation of momentum and energy. Let's consider a classical collision model

well known from billiard: energy and momentum are transferred from the moving ball to the stationary target ball. Incident particle of mass M_1 is moving with velocity v, thus carrying kinematic energy $E_0 = \frac{1}{2}M_1v^2$ while the target atom of mass M_2 remains stationary. After the collision takes place the projectile is scattered from the incident trajectory into angle ϑ, called scattering angle. Target atom is recoiled from its original position into recoil angle φ. The respective resulting values for velocities v_1 and v_2; and energies E_1 and E_2 of colliding participants are determined by scattering and recoil angles. The geometry with respect to the laboratory system of coordinates, and with the notation used above, is given in Fig. 1.1.

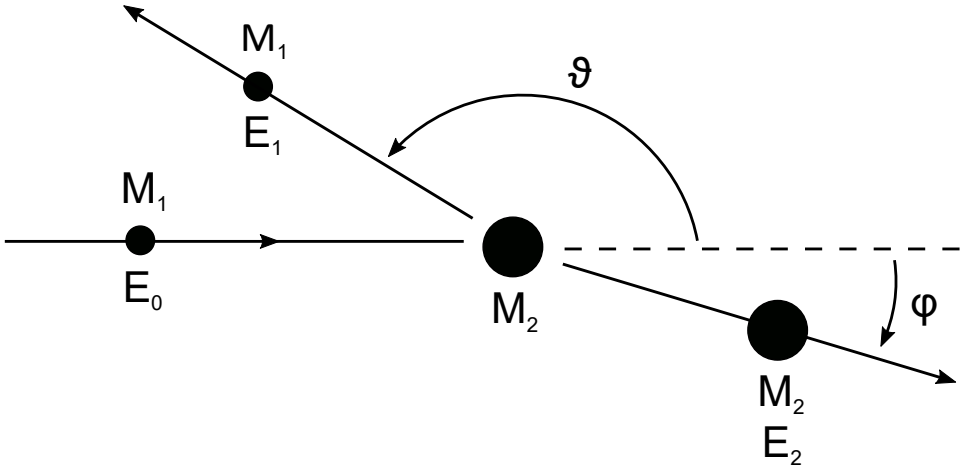

Figure 1.1: Schematic of a binary collision, where the projectile of mass M_1 and energy E_0 is scattered into angle ϑ from a still target atom with mass M_2.

The energy conservation and conservation of momentum in parallel and perpendicular direction to the incidence are expressed by equations:

$$\frac{1}{2}M_1v^2 = \frac{1}{2}M_1v_1^2 + \frac{1}{2}M_2v_2^2 \tag{1.1}$$

$$M_1v = M_1v_1\cos\vartheta + M_2v_2\cos\varphi \tag{1.2}$$

$$0 = M_1v_1\sin\vartheta - M_2v_2\sin\varphi \tag{1.3}$$

Eliminating first the angle φ from Equations 1.2 and 1.3 and then the parameter v_2 the ratio of particle velocities is found to be:

$$\frac{v_1}{v} = \left[\frac{\pm\left(M_2^2 - M_1^2\sin^2\vartheta\right)^{\frac{1}{2}} + M_1\cos\vartheta}{M_2 + M_1}\right]. \tag{1.4}$$

The energy ratio for the case $M_1 < M_2$ where only plus sign remains is

$$\frac{E_1}{E_0} = \left[\frac{+\left(M_2^2 - M_1^2\sin^2\vartheta\right)^{\frac{1}{2}} + M_1\cos\vartheta}{M_2 + M_1}\right]. \tag{1.5}$$

The projectile energy ratio, called the *kinematic factor* $K = \frac{E_1}{E_0}$, shows that the proportional energy of the scattered particles is determined only by masses of incident and target

atoms; and by scattering angle. Extreme of the function i.e. the minimum value corresponds to the maximal energy transfer to the target atom. This happens under scattering angle 180 °, where we are talking about so called direct backscattering. Kinematic factor is for this case proportional to:

$$\frac{E_1}{E_0} = \left(\frac{M_2 - M_1}{M_2 + M_1}\right)^2. \tag{1.6}$$

A single collision with large-angle scattering outcomes not only establishes the described model, but also gives basis to the modern analytic technique Rutherford Backscattering Spectrometry (Sec. 2.2.1).

While the incident particle is scattered by target the atom the transferred energy causes the deflection of target from its rest state into recoil angle. Gained impulse is proportional to the fraction of incident energy of projectile given by general relation:

$$\frac{E_2}{E_0} = \frac{4M_1M_2}{(M_1 + M_2)^2}\cos^2\varphi. \tag{1.7}$$

The amount of energy transferred to the target atom is highly increased when heavy elements are used as a projectiles. Moving recoiled atom then becomes a new projectile for its immediate surrounding. Under certain geometric circumstances the recoiled atom can be directed into forward way and ejected from sample; also know as Elastic Recoil Detection Analysis (Sec. 2.2.3). Numbers of collision events can also occur during recoil, passing through the surrounding area, and this collision cascade can, in final step, eject the atom out of the surface. This described process is called sputtering and provides the basis for analytic technique Secondary Ion Mass Spectrometry (Sec. 2.2.5).

1.2. Cross section

Identification of the target atom is established by the measured energy of scattered projectile into scattering angle ϑ. The number of target atoms N_s per unit area is determined by the probability of collision between projectile and target atoms measured as the number of detected particles Q_D out of the total number of incident particles Q. The connection between the N_s and Q_D is described by *scattering cross section* $\sigma(\vartheta)$. In general the scattering cross section in given in differential form $\frac{d\sigma(\vartheta)}{d\Omega}$, where $d\Omega$ represents the differential solid angle centred about ϑ. For the small detector area A in distance l from the target the solid angle Ω has a form A/l^2 and the differential cross section can be averaged:

$$\sigma(\vartheta) = \frac{1}{\Omega}\int_{\Omega}\frac{d\sigma}{d\Omega}d\Omega. \tag{1.8}$$

The relation between the number of target atoms/cm^2 and yield of detected particles Q_D follows the equation

$$Y = Q_D = \sigma(\vartheta)\Omega Q N_s. \tag{1.9}$$

Parameter Q can be directly derived by time integration of collected charge in the sample or by the indirect way described in Section 3.1.

To calculate the scattering cross section, we will leave the billiard model and take into consideration the real atom nature i.e. the Rutherford model with positively charged

nuclei placed in the middle of the surrounding electrons cloud. The repulsion of projectile from target can be described as a force that acts during the close approach of particles. In most cases of backscattering it is presumed that projectile has sufficient energy to penetrate the electron cloud of the target atom and approaches its nuclei in distance well within the electron orbit. Hence the acting force can be described as unscreened Coulomb repulsion of two positively charged nuclei with atomic numbers Z_1 and Z_2. The atomic number gives the information about number of protons in the nuclei and thus its overall charge. Let us first explore this unscreened cross section for its simplicity; and, afterword, add the screening as a correction to obtained results.

It is practical to start with the central force model; where the two-body problem is simplified into one-body. Deflection of the projectile in one-body formulation is treated as a scattering from the force acting in the centre of the coordinated system. It would represent the system where $M_1 << M_2$. The central force scattering ensures the conservation of kinetic energy and complete symmetry around the axis of the beam. Defining the impact parameter b, the perpendicular distance between projectile incident trajectory and parallel line coming through the centre point shown in Fig. 1.2, the relation for scattered trajectory can be found as

$$2\pi b\, db = -\sigma(\vartheta) 2\pi \sin\vartheta\, d\vartheta. \tag{1.10}$$

Distribution of particles with an impact parameter of between b and db; scattered into angles ϑ and $d\vartheta$ is only related by the scattering cross section, where a minus sign reveals that the further the projectile is from nuclei, the acting force is correspondingly weaker; and thus the final scattering angle decreases.

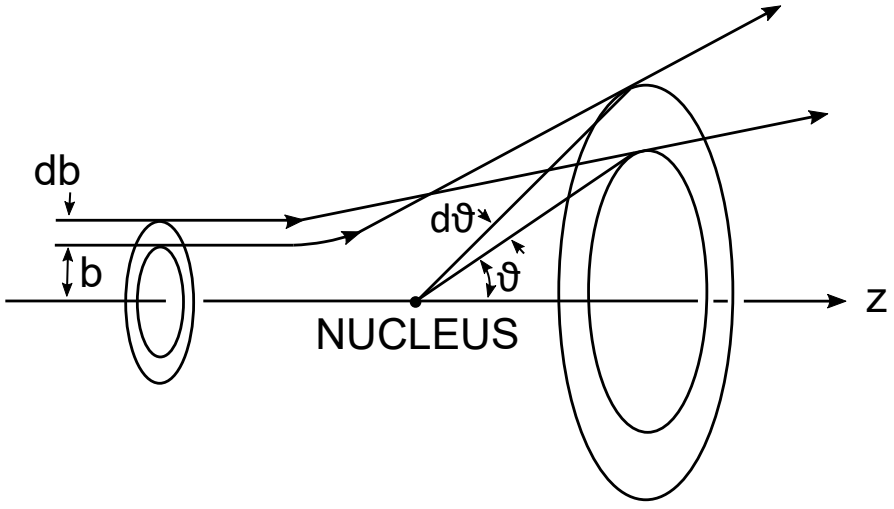

Figure 1.2: Schematic illustrating the number of particles between b and db being deflected into an angular region $2\pi \sin\vartheta\, d\vartheta$. The cross section is, by definition, the proportionality constant; see Eq. 1.10. Adapted from [3].

Particle with the charge $Z_1 e$ approaching the target nuclei with the charge $Z_2 e$ will at distance r experience a repulsive Coulomb force,

$$F = \frac{1}{4\pi\varepsilon_0} \frac{Z_1 Z_2 e^2}{r^2}, \tag{1.11}$$

which will cause the trajectory to deviate from a straight line path (Fig. 1.2). The initial p_1 and final p_2 particle momentum have an unchanged magnitude, but different direction. The total change $\triangle p$ by acting force F is

$$\triangle p = p_2 - p_1. \tag{1.12}$$

The step by step derivation can be found in [3], where the force $F = \frac{dp}{dt}$ is integrated along the particles trajectory. Resulting Equation 1.13 relates the momentum change with the impact parameter found in Eq. 1.10:

$$\triangle p = 2M_1 v \sin\frac{\vartheta}{2} = \frac{Z_1 Z_2 e^2}{vb} 2\cos\frac{\vartheta}{2}. \tag{1.13}$$

By combination of given equations the form of Rutherford scattering cross section is found:

$$\sigma(\vartheta) = \left(\frac{Z_1 Z_2 e^2}{4E}\right)^2 \frac{1}{\sin^4\frac{\vartheta}{2}}. \tag{1.14}$$

This scattering cross section predicating E^{-2} and $\left(\sin^4\frac{\vartheta}{2}\right)^{-1}$ dependence of scattered amount, originally derived by Rutherford, was experimentally verified in the beginning of the 20^{th} century.

Until this point it was presumed that the energy of the projectile is conserved. However, from the Section 1.1 we have learnt that elastic collision leads to energy transfer to recoiled atom. Incident particle loses its energy according to the kinematic factor, from Eq. 1.5, and it is the observed change that carries the information about the target. The fact that the target atom recoils from its initial position undermines the one-body problem and has to be considered for correct evaluation of scattering cross section. However, the new problem of two body central force can be reduced back into one-body problem by the trick when mass M_1 is replaced by the reduced mass $\mu = M_1 M_2/(M_1 + M_2)$. The scattering angle also then differs from the one found in Eq. 1.14 but after transformation the cross section has its final form:

$$\sigma(\vartheta) = \left(\frac{Z_1 Z_2 e^2}{4E}\right)^2 \frac{4}{\sin^4\vartheta} \frac{\left(\left\{1 - [(M_1/M_2)\sin\vartheta]^2\right\}^{\frac{1}{2}} + \cos\vartheta\right)^2}{\left\{1 - [(M_1/M_2)\sin\vartheta]^2\right\}^{\frac{1}{2}}}. \tag{1.15}$$

In case of backscattering the applied transformation brings the correction in units of percent. However, the correction is very appreciable for scattering from light element and for accurate quantitative analysis.

The described Rutherford model works for wide range of energies (MeV), but has its limitations. We assumed that the projectile velocity is sufficiently large to penetrate inside the electron orbits and, therefore, that scattering is then based on the unscreened Coulomb repulsion of two positively charged nuclei of atomic number Z_1 and Z_2. For the Coulomb potential $V(r)$ to be valid the closest approach between nuclei has to be lower than the most inner electron radius. In small-angle scattering, low-energy or heavy particle collision this condition would not occur. Incomplete penetration through the electron shells

would lead into screening of the target nuclei charge by the innermost electrons. The real screened potential that particle experience can differ from the Coulomb example in orders of magnitude. Correction is made by multiplying Coulomb potential by *screening function* $\Phi\left(\frac{r}{a}\right)$, where r is the distance between particles and a so called *screening length*. At present, however, there is no uniform expression of screening function for general collision of two particles. Few expressions were derived based on various electron orbit models like Moliere-Thomas-Fermi, Firsh, Linhard, etc. However, it is generally known that these expressions for screening function do not suit all combinations of projectiles and target atoms. These deviations can be corrected by introducing the correction factor c_F into the shading length relationship. More about this correction can be found in article [4]. Ziegler, Biersack, and Littmark have suggested an expression for interaction potential, which is abbreviated as ZBL potential. This potential was designed by fitting universal screening functions on the theoretically obtained interaction potentials calculated for a wide range of atoms pairs. The ZBL potential screening function has the form [5]

$$\Phi(x) = 0.1818e^{3.2x} + 0{,}5099e^{0.9423x} + 0.2802e^{4.4029x} + 0.02817e^{0.2016x}, \tag{1.16}$$

where $x = \dfrac{r}{a_u}$ and a_u is the screening length for ZBL interaction potential

$$a_u = \frac{0.8854}{Z_1^{0.23} + Z_2^{0.23}}. \tag{1.17}$$

The other extreme of departure from Rutherford scattering cross section can appear at high energies and small impact parameter, where the particle interacts with the target nuclei. Deviation from Rutherford scattering due to nuclear interaction becomes important when the closest approach is comparable to nuclei radius R. With certain energy the interaction leads to strong increase (resonance) in scattering cross section and thus the higher sensitivity can be reached. Analytical method based on this principle is called Elastic backscattering spectroscopy (Sec. 2.2.2).

1.3. Stopping power

In previous section we assumed that atoms, to be identified, were present only at the surface of the material. If it is only the nucleus, plotted in Fig. 1.2, that interacts during the collision it is obvious that the projectile can easily miss the target. The radii of atomic nuclei are, in comparison to atomic dimension, small. We have already found the parameter that corresponds to the probability of collision; the scattering cross section. Dependence on inverted squared energy of the projectile implies that low mass, high energy projectiles can penetrate to the solid. In this section we will describe the processes that accompany the projectile passage through the solid; and thus give the basis to the depth profiling.

As the light particle penetrates through the solid it loses energy predominantly through the excitation and ionization of target atomic electrons during inelastic collisions. From a microscopic point of view the electronic excitation and atomic ionization is a discrete process, which also forms a basis for the technique Particle Induced X-ray Emission (Sec. 2.2.4). Macroscopically the continuous energy loss can be assumed as we are concern only in average energy loss during the projectile penetration into solid. Since the projectile in the sample undergoes many collisions with electrons and can be ionized multiple

times during its flight, it is very difficult to describe all possible interactions for all states of the projectile ionization. Therefore, the *electron stopping power* is defined as a function of energy, which expresses the average energy loss caused by interactions with electrons per unit length along the trajectory of the incident particle:

$$S_e(E) = -\frac{dE_e}{dx}, \tag{1.18}$$

where E is the energy and x the projectile path. Stopping power can also be found in combination with atomic density $(\frac{1}{N})(\frac{dE}{dx})$ [eV/(10^{15} atoms/cm^2)] , where we are talking about the *stopping cross section* ε. Fig. 1.3 shows the energy-loss components for the particle scattered from the depth d.

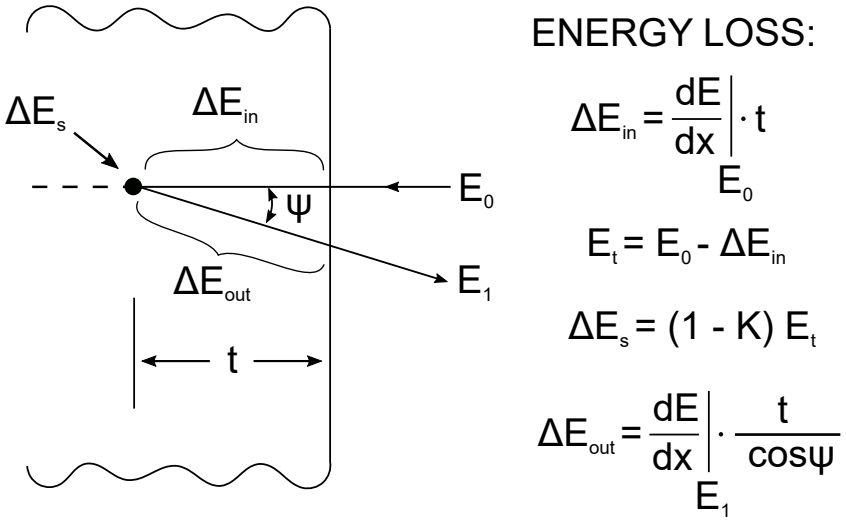

Figure 1.3: Energy-loss components for a projectile that scatters from depth t. The sequence is: energy lost via electronic stopping on inward path $\triangle E_{in}$; energy lost in the elastic scattering process, $\triangle E_s$; and energy lost to electronic stopping in the outward path, $\triangle E_{out}$. Then $E_1 = E_0 - \triangle E_{in} - \triangle E_s - \triangle E_{out}$. Adapted from [3].

Section 1.1 describes the interaction between projectile and target nuclei, which results in large-angel scattering. We have also found that the projectile does not always attain sufficient distance for this radical interaction to happen. Coulomb potential is screened by the electron orbits and interaction outcomes are much weaker. However, according to the Eq. 1.5, a fraction of the projectiles kinetic energy is still transferred to the target. Hence, the particle passing along the target's nuclei is moreover slowed down by the so called *nuclear stopping power*; the total stopping effect being a simple sum of the stopping effects of electrons and nuclei

$$S(E) = S_e(E) + S_n(E). \tag{1.19}$$

At the beginning of the projectile deceleration process, the projectile is slowed primary by the electron stopping force. The slower the projectile is, the more likely the collisions with the atomic nuclei begins to dominate. The stopping power of the nuclei increases with the increasing weight of the projectile M_1 and decreases as its energy E_0 increases (see Figure 1.4).

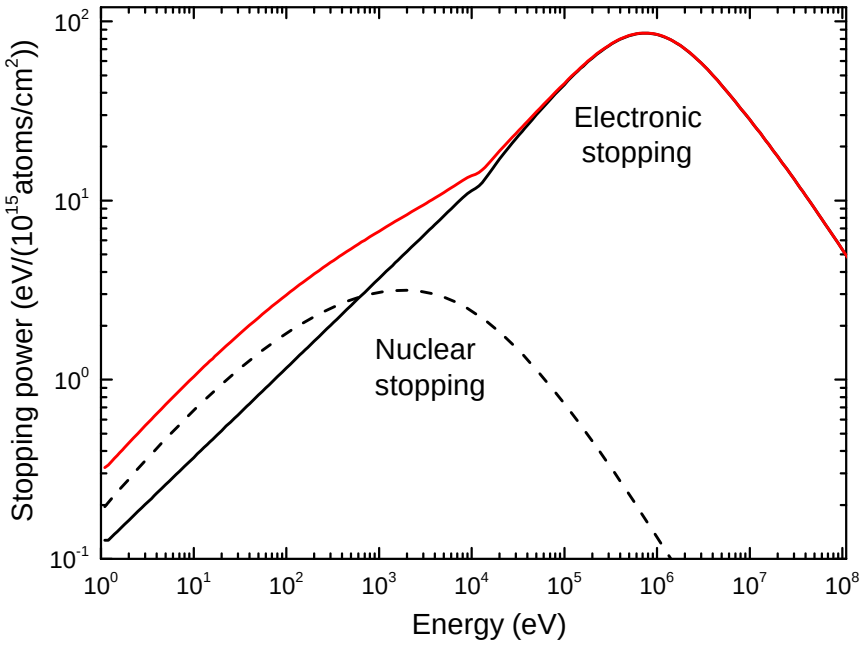

Figure 1.4: Stopping power as a function of incident ion energy. As an example, the stopping of helium in iron was simulated with SRIM [6]. Nuclear stopping (dashed curve) dominates only at low energies. The electronic stopping curve (solid) exhibits a clear maximum, which is called Bragg peak.

The stopping power of electrons can be calculated with an accuracy of several percent for projectile energies greater than several hundred keV. For energy of the projectiles lower than $\approx$ 100 keV, the calculation is more complex and the results are not sufficiently accurate. In addition, the stopping power of electrons, for different combinations of the projectile and the target atom, strongly changes. Therefore, the stopping power of electrons is usually empirically or semi-empirically determined [7, 8].

For a target that contains more that one element the stopping power is calculated as a sum of losses on individual constituent elements weighted by the abundance of the element. This postulate, called *Bragg's rule*, states that the stopping cross section $\varepsilon^{A_m B_n}$ of a solid of composition $A_m B_n$ is given by (for further discussion see [9]):

$$\varepsilon^{A_m B_n} = m\varepsilon^A + n\varepsilon^B, \tag{1.20}$$

where ε^A and ε^B are the stopping cross sections of the atomic constituents A and B.

2. Techniques and instrumentation

2.1. Ion sources

For calculations in the previous chapter we have mostly referred to the incoming particles simply as projectiles being stripped of their true nature. Let be reminded that during all this time the colliding particles were ions of various masses and charges. There is an entire research area behind the ion sources describing the ion creation processes. In the following section the basic principles of sources used in this thesis will be briefly introduced. Further information can be found in [10].

When an electron strikes a target atom or molecule, there is a chance that during the impact, one or more electrons are removed from the target particle. Atom or molecule is then turned it into an ion. Ion sources using electron impact ionization works in practice by supplying electrons (typically from a cathode) accelerated to an energy sufficient to cause ionization of the material in a chamber. Created ions are then extracted by an external field.

Based on a similar principle of electron ionization, another ion source creates a plasma as the density of ions and electrons in the source increases. The creation of significant numbers of ions and electrons from the initial gas will lead to the potential of sustaining a discharge (overall charge of electrons and ions in plasma is zero). The advantage of these electrical discharges is that they contain large quantities of ions that can again be extracted as an ion beam.

The charge-exchange ion source uses the transfer of electrons directly between ions and neutral atoms and molecules. The positively charged ions from the first stage pass through a charge-exchange cell, which should contain the gas or alkali vapour that will serve as the electron donor. The polarity of the incoming ion is changed to negative.

Ions can also be extracted from the solid or liquid material. It is usually done by combination of two materials, where one steals the electrons from another and thus increase the probability of ion desorption. Liquid Metal Ion Gun (LMIG) uses the metal melted at the heated sharp wolfram tip. Strong electric field creates a jet of charged particles emanating from the tip.

2.2. Analytic techniques

2.2.1. Rutherford Backscattering Spectrometry

Rutherford Backscattering Spectrometry (RBS) represents the perfect example of adopting described collision theory into practice. Moreover, it was Rutherford who, by following his golden foil experiment, gave theoretical basis to modern nuclear physics. Hence, while the other technique are carrying the names connected to the essences of methods,

the Rutherford's contribution gave him the privilege of calling the technique Rutherford backscattering. However, literature also describes the term HEIS (High Energy Ion Scattering).

Sample is irradiated with the beam of energetic light ions (usually $2-3\,\mathrm{MeV}$ H^+ or $He^{+,++}$) and the elastically backscattered projectiles at large angles are detected. The energy loss of a backscattered ion is dependent on two processes: the energy loss in scattering events with sample nuclei, and the energy loss due to interaction with target electrons. The first process is dependent on the scattering cross section (Eq. 1.14) of the nucleus and thus on its mass M_2 and atomic number Z_2. Binary collision between ion and target takes place and as they approach each other elastically scattered particle suffers energy loss according to kinematic factor K (Eq. 1.5). For a given measurement angle, nuclei of two different elements will therefore scatter incident ions to different degrees and with different energies. To distinguish between close-mass elements $\triangle M$, the maximum energy transfer is required. Kinematic factor minimum (Eq. 1.6) is reached during so called head on head collision under scattering angle $\vartheta = 180°$. Note that the probability for scattering to this angle is the lowest. However, considering the number of incident projectiles coming through the beam (billions within few seconds), the sacrifice of the yield for the mass resolution is reasonable. Separate peaks on an $Y(E)$ plot of measurement counts versus energy (see Eq. 1.9) are produced by particle detection. These peaks are characteristic of the elements contained in the material and provide a means for analysing the sample composition. The scattered energy is matched with the known scattering cross sections and relative concentrations can be determined by measuring peak heights.

The second energy loss process is the stopping power of the sample electrons described in Section 1.3. This interaction doesn't lead to large discrete losses, such as those arising from nuclear collisions. Instead, it produces a gradual loss of energy, depending on the electron density and the distance that ion travels through the sample. This energy loss reduces the measured particle energy depending on the depth of the nuclei inside the sample, from which it is backscattered. As a result, instead of sharp backscattered peaks in the $Y(E)$ plot, the observed peaks gradually decrease towards the lower energy because of the ions passing through the sample. If the elements appear only at particular depth of the sample their peak positions will be shifted by a correspondingly particular amount that relates directly to the distance the ion must pass to reach the nuclei. Generally the stopping power is given rather in thin film units, i.e. $\mathrm{eV}/(10^{15}\ \mathrm{atoms/cm^2})$ since the density of the material may vary as a function of thickness. Experimental data measured on he majority of materials were collected within one shared database SRIM (Sec. 2.3.2). Stopping power is nowadays known for all materials at around 2 %. In case of compounds the Bragg's rule (Eq. 1.20) is used.

The RBS method is however challenged on other levels. By example two identical energy particles having the same initial velocity do not have exactly the same energy after passing through the medium. The loss of energy E is subject to fluctuations thanks to many individual encounters during the passage. This phenomenon is called *energy struggling*. The energy struggling gives the ultimate limit of accuracy with which energy losses and hence depth can be resolved. Together with detector resolution these two contribution give the total energy resolution δE_1:

$$(\delta E_1)^2 = (\delta E_D)^2 + (\delta E_S)^2. \tag{2.1}$$

Low resolution often restricts the detection of heavy close-mass and light elements present in heavy matrices. Matrix effect generally introduces many complications into analysis; as will be discussed later. However RBS is more less immune to these complications; and is thus fully quantitative. The matrix effects play a role only in crystalline samples where so called *channelling* occurs under circumstances where the sample crystal lattices are aligned with projectile incidence. Ions then travel deep into the sample without meeting a nucleus to be scattered from and, thereby, signal changes. However, by taking advantage of channelling it is possible to learn something about the crystal structure as a kind of spatial information. More about RBS and its different features can be found in [11].

2.2.2. Elastic Backscattering Spectrometry

As we have discussed in Section 1.2, that the incident ions can, under certain elevated energies above those normally used in RBS, overcome the Coulomb barrier. These particles would, under resonance conditions for a sharply defined resonance energy, undergo a nuclear reaction with the target nuclei. The reaction product is usually a nucleus in an excited state that immediately decays, which produces emitting ionizing radiation (can be both particle and photon). The event is mostly inelastic because Q^* [1] value is not zero. Methods using nuclear reactions and its products, for compositional depth profiling, are Nuclear Reaction Analysis (NRA) and Particle Induced Gamma Emission (PIGE). This reaction cannot be equated with Rutherford's backscattering theory because the derived cross section in Eq. 1.14 is based on elasticity ($Q^* = 0$). However, the non-Rutherford cross sections can also be resonant. Method based on this principle is called Elastic (non-Rutherford) Backscattering Spectrometry (EBS) [12]. Although this process loses the simple energy and charge relationship in cross section, it has the potential to considerably enhance the cross sections above Rutherford's values for light elements; and thus make it possible to quantify/profile these elements in the heavy matrices. The EBS method is widely used for probing light elements as N,C,O where the resonance takes place at accessible energies to the extent that the interactions with the heavier elements remain Rutherford. For example, the helium nuclei-oxygen reaction ($^{16}O(\alpha,\alpha_0)^{16}O$) has a strong and very useful narrow resonance at 3037 keV. To obtain a real scattering cross section for non-Rutherford interaction the Schrödinger's equation should be solved. SigmaCalc [13] provides the computed cross sections as well as a database of experimentally derived cross section for various particles, energies and scattering angles [14]. The example of scattering cross section for oxygen and helium projectile, including the mentioned resonance at 3037 keV, is shown in Fig. 2.1.

[1] The Q^* value for a reaction is the amount of energy absorbed or released during the nuclear reaction.

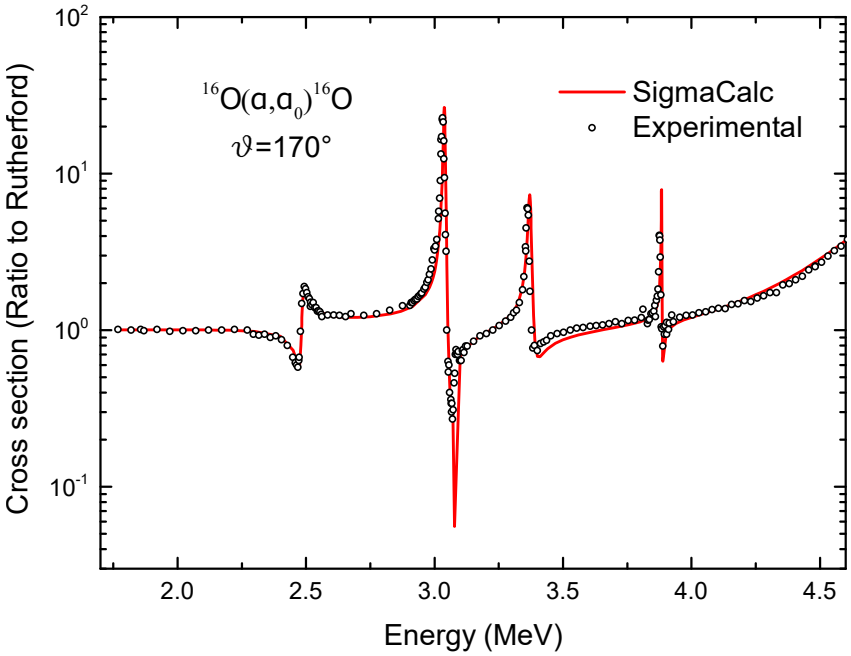

Figure 2.1: Deviation from Rutherford cross section as a function of energy for elastic scattering of He^+ from oxygen. The red continuous curve shows the anomalous cross section dependence (resonance) at 3037 keV. Experimental data from [15] (open circles) are also displayed for comparison.

To contribute to the nuclear reaction the projectile have to slow down in the sample to reach the resonance energy. Thus each initial kinetic energy corresponds to a depth in the sample where the reaction occurs (the higher the energy, the deeper the reaction).

2.2.3. Elastic Recoil Detection Analysis

In a single elastic collision, momentum considerations prevent the scattering of projectile ions in reverse directions when $M_1 > M_2$. The incident energy is transferred primarily to the lighter target atom in a recoil collision (Eq. 1.7). The great advantage of this can be utilized by using forward scattering geometry. This means placing the target at a glancing angle with respect to the beam direction and by moving the detector to a forward angle (see Fig. 3.1). Under this geometry one can detect forward-scattered heavy projectiles and recoiling atoms from a single collision. The detection of elastically scattered recoils is the basis for ERDA [16]. Due to the irradiation with heavy primary ions with several tens of MeVs, the cross section for recoils is approximately proportional to Z_2/M_2 and, therefore, almost constant. This implies that the recoil cross section does not decrease dramatically for light elements as in RBS (Eg. 1.14) and, moreover, gives almost equal sensitivity for all constituents. The uniqueness of the ERDA technique comes from the privilege of measuring the hydrogen content in thin films with detection limit ±0.01 atomic %. Recoils ejected from certain depths up to 1 µm are loosing gained energy during their passage towards the surface. The mass resolution for heavy elements is rather poor in comparison to the light elements, where quantitative elemental depth profiling is possible. The mass-separation of the recoiled ion species is accomplished by measuring their Time of Flight (ToF) and energy in coincidence (ToF-E). Detection of both energy and ToF allows for extracting the depth information carried by recoiled particle. When

using heavy ion beams, care must be taken for beam-induced damage in sample such as sputtering or amorphization.

2.2.4. Particle Induced X-ray Emission

Energy loss of particle travelling through the matter (Sec. 1.3) is driven by excitation of targets electron structure. Bohr's and quantum theory states that within any stable atom electrons must maintain constant energy levels (stationary states). The accelerated particle beam carries sufficient energy to excite the inner shell electrons and thus disrupt this stability. In turn, to maintain equilibrium, outer shell electrons decay to fill the vacancy from excited inner-shell electrons and subsequently X-rays are emitted. The first three atomic discrete energy levels where the transitions take place are represented by electron shells called K, L, M (see Fig. 2.2).

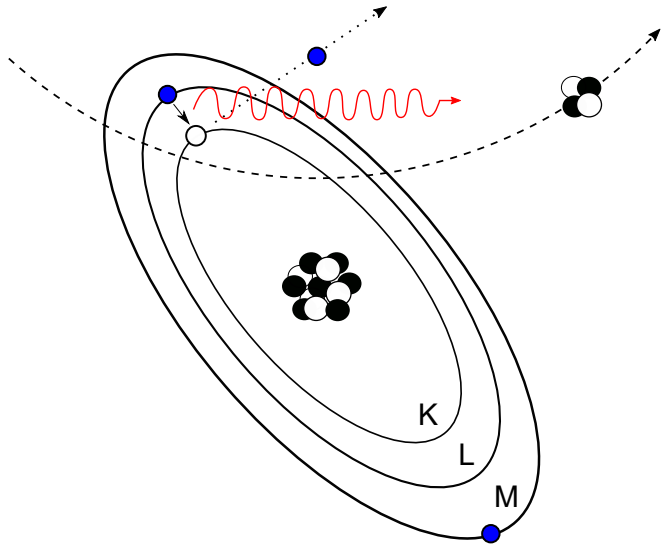

Figure 2.2: Basic principle of PIXE. Schema indicates ion interaction with inner shell electron causing the emission of electron. Consequential hole filling from outer shell electron is accompanied by X-ray radiation emission.

While only discrete transitions between energy states are possible, the energy emissions are characteristic of independent elements. The detected X-ray energy spectrum consists of a continuous background along with the characteristic X-ray peaks of the atoms present in the sample. The yield of characteristic X-ray is proportional to the elemental concentration in the material. The transitions going to the K shell are indicated as K X-rays. When the vacancy is filled by an electron coming from the L shell, the transition is denoted as K_α, and when it comes from the M shell, K_β.
The cross section of this process is called the *ionization cross section*. It is a probability that measures how many ionization event occur. The cross section for inner K-shell ionization by the impact of proton or helium ions is generally calculated using the theoretical method known as Plane Wave Born Approximation (PWBA) based on perturbation theory. The L-shell case is relatively more complicated than the K-shell case and is treated by Brandt and Lapicki's ECPSSR method using statistical methodology. More about calculation of ionization cross section can be found in [17]. The probability of a consequential emission of an X-ray quantum (the *fluorescence yield*) is close to 1 for the heavy elements; but only a few percent for the light elements.

The biggest advantage of PIXE comes from the high sensitivity for heavier trace elements, where the characteristic peaks are well separated, even for near-mass elements. The limitations are primarily in regards to which elements it can identify. PIXE is accurate for elements above sodium. Anything below sodium will be absorbed prior to reaching the detector. This phenomena also doesn't allow for the depth profiling as the X-ray passage from the sample is the subject of complicated processes.

2.2.5. Secondary Ion Mass Spectrometry

Until this point the described techniques were referred to as high energetic where, to some extent, the interaction processes could be described by simple models; and where atomic quantification (from IBA) is possible. Low energetic technique, as are the Low Energy Ion Scattering (LEIS), and Secondary Ion Mass Spectrometry (SIMS) are challenged in many levels. In the the Chapter 1 we discussed that for lower projectiles energies the coulomb interaction is screened by atomic electron structures; and so the simple model requires corrections. In general the low energy and higher projectile mass leads to strong increases of scattering cross section (Eq. 1.14); and thus the interaction with the target takes place close to the surface.

The bombarding ion transfers energy in collisions to target atoms that recoil with sufficient energy to generate further recoils. Some of these backward recoils will approach the surface with enough energy to overcome the surface barrier and escape from the solid. The sputtering process involves a complex series of collisions (the collision cascade) involving a series of angular deflections and energy transfers between many atoms in the solid. Surface layers are eroded by the sputtering process, hence the relative abundance of the sputtered species provides a direct measure of the composition of the layer that has been removed. The majority of sputtered species are emitted as neutrals. Only a very small portion leaves the surface as ions. The probability of knocking off the sample atom is given by *sputtering cross section* whose derivation is difficult even for single element, amorphous sample and becomes rather impossible for compounds. The ratio of ionized to neutral species from the same sample can vary by orders of magnitude. Both positive and negative, singly and multiply charged; and as ionized clusters of particles are formed close to the surface during the sputtering, depending on the condition of the surface. Secondary ion yields are very sensitive to the presence of either electro-positive or electro-negative atoms at the target surface. This strong dependence on the sample structure and the materials surrounding the sputtered particle is well known as *matrix effect*. The matrix effect is possibly the most significant unresolved issue that doesn't allow for the quantification. Detailed description of the SIMS technique discussing all its principles and challenges can be found in [18].

Various combinations of primary beam ions and sputtering energies are adjusted depending on the depth of interest and on particular information to be gained. Modern SIMS instruments operating in number of modes: compositional imaging with good lateral resolution (50 nm), spectrometry with enhanced mass resolution and high resolution depth profiling. The sample surface is exposed to a high dose of energetic incident ions, where the sputtering leads to the formation of crater. At the same time, when the sample material is sputtered, primary ion beam ions are implanted. The primary ions and the sample material are mixed in this process and after some time a (dynamic) equilibrium is established, which is characterized by a constant sputtering rate and the formation of an altered layer. The presence of implanted primary ions can cause an enhancement of secondary

ion yield. In the formed crater the area of interest is then rastered by precisely focused ion beam and sputtered ions are further analysed by mass spectrometer (Sec. 2.3.1). Sputtered ions (among other emissions as e.g., neutral atoms and molecules) are predominately emitted from the first few sub-atomic monolayers, which makes the SIMS the most sensitive of the surface-analysis techniques.

2.3. Detection and analysis

2.3.1. Detectors

To allow for the detection of various reaction's products described in Section 2.2, the system of detectors has to be incorporated in the experimental set-up. As the product, i.e. particle or radiation carries the seek information about sample its nature and origin defines the convenient geometry and method for the information to be gained. During the beam-solid interaction the space above the sample surface is filled with a variety of interaction products. However some directions are more convenient to be used for detection. In the case of perpendicular orientation of beam towards the sample surface, the particles are scattered with highest probability into scattering angle about 110° in respect to the beam. Nevertheless, the high yield doesn't come with good mass resolution. It can be only achieved by maximizing the change in projectiles momentum (Eq. 1.6). Hence, the best energy resolution can be achieved by placing the detector close to perpendicular position. The situation is different for X-ray where the good yield is advantageous. Characteristic X-ray emitted from the sample in given geometry is conveniently acquired under angle 135° in respect to the beam. In both cases the Solid State Detectors (SSD) are used. To avoid mismatch and possible damage by acquiring the undesired product of beam-sample reaction, some method of filtering has to be included. While X-ray radiation ranges in tens of keV it is buried deeply in RBS's Mev spectra background. Contrary hereto, the opposite would not allow for detecting any X-ray. Thus, foil thick enough to stop backscattered particles, and at the same time, transparent for radiation has to be used. Special attention is required for the recoil measurement where the products of collision are sputtered into grazing angles together with scattered incoming high energetic projectile. The resulting wide particles energy range would be critical for SSD thus the ionization chamber is rather used. In general there are two approaches on how to best gain information from a particle, i.e. to measure particle energy and, separately, to measure its time of flight through the detection system.

Solid State Detectors

The solid state detector is the most commonly used device for detection of the charged particles like protons and alpha as well as for X-ray radiation. Semiconductor material such as silicon crystal constitutes the detecting medium. It consists of p-n junction, the interface between two different semiconductor materials called p-type and n-type. Those are formed by deliberate addition of impurities into pure silicon crystal. P-type semiconductor contains of vacancies in electronic structure called holes that simulate the positively charged particles, whereas the n-type contains free electrons. Applying the bias to the junction in forward or reverse direction the electric current respectively flows across the junction or doesn't. The simplest device working on this principle is diode.

Ionizing radiation passing through the device generates an electron-hole pairs in semiconductors bulk. These charge carriers migrate towards the opposite faces of the block under influence of applied bias and creates the current pulse. The pulses are amplified, recorded and analysed in order to determine the number and energy of the incident particle or radiation. SS detectors are often challenged in term of energy resolution and counting rate.

Silicon Drift Detector

To meet a sufficient energy resolution and counting rate for X-ray detection, where the necessity for resolution is obvious comparing from the RBS and PIXE energy ranges, the devices called Silicon Drift Detectors were developed. The basic form was proposed by Gatti and Rehak [19] in 1984 where the biased field strips create the electrical field parallel to the surface guarding the signal charge towards the collecting anode. Modern devices with cylindrical design allows of integrating reading electronic with cooling directly on the chip. The detector has unique features that satisfy all these requirements. Moreover, it attains high quantum efficiency at both the lowest and highest X-ray energies [20]. The Figure 2.3 shows the cross section of cylindrical silicon drift detector.

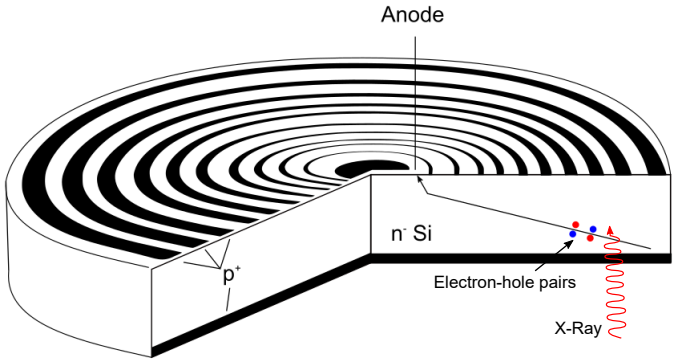

Figure 2.3: Cross section of a cylindrical silicon drift detector. The acquisition chain is connected to the collecting anode. The radiation entrance window for the ionizing radiation is the non-structured backside of the device. Adapted from [20].

Gas ionization chamber

Radiation detected by penetrating the solid semiconductor crystal is decelerated by its structure due to the collisions. No actual harm is caused to the detector while the projectiles are much lighter then silicon atoms. Radiation damage would take place if the detector was bombarded by heavy charged particles. To allow for detection of heavy particles the same principle of creating the charged pair can be adopted into different detecting mediums. The simplest construction of Gas Ionization Chamber (GIC) consist of two electrodes in the chamber filled with gas. When the gas is ionized by incident radiation the ion-electron pairs are created. Resultant positive ions and dislocated electrons drift towards the electrodes with opposite polarity and their charge is collected and amplified. Thanks to the well known stopping power of the gas many various designs of chamber and collection electronic have been developed in order to provide ion separation and to meet a good energy resolution [21].

Micro-channel plates

To detect an event such as the single charged particle collision, either the collecting anode has to be properly shielded from any source of noise or charge multiplication devices as Micro-Channel Plates (MCP) are used.

The MCP detector consists of few $\approx 14\,\mathrm{mm}$ cylindrical plates, where each plate contains a plurality of miniature channels connected to each other. These channels are made of a material with a high secondary emission coefficient so if particles fall on the inner wall, the secondary electrons are emitted. As they travel through the channel, they strike the walls of the channel and thus emit more electrons. The front and back walls of each plate are covered with a layer of conductive material. Different electrostatic potentials are introduced to the electrodes for acceleration of the ejected secondary electrons and thus provide them sufficient energy to punch out other secondary electrons. The electron current gradually increases in avalanche. Usually, multiple consecutive plates are used in series. This leads to a gain of the current in the order of 10^7. Behind the plates an anode collects the pulse.

Time of Flight detection

Another property of the particle is its time of flight (ToF). Measuring the time that particle needs to travel through fixed distance can provide valuable information about its origin. From the simple kinematics the moving particle carries the energy

$$E = \frac{1}{2} \cdot M \cdot \left(\frac{d}{t}\right)^2, \tag{2.2}$$

where M is mass of the particle and fraction of distance and time is its velocity. While time is measured on given distance, the mass and energy can be derive from equation with the additional knowledge of one remaining parameter. In general the time is measured between two events along the particles trajectory.

An obstacle formed by very thin carbon foil (units of $\mu\mathrm{g/cm}^2$) allows for the register of the particle passage. Electrons ejected during the transfer are accelerated towards MCPs where a pulse is created. The same event takes place at the second foil distant from the first one and the time spread of pulses is analysed. It is worth mentioning that incident energy of particle passing through the foils is changed with well estimated amount that is, in the most of the application, negligible in comparison to the energy detector resolution. Controlled modification of the incident particle energy leaves the mass in Eq. 2.2 to be only variable; and thus gives the basis for the method called ToF mass spectrometry.

Mass spectrometrer

The ToF mass spectrometer uses an electric field to accelerate the ions through the same potential; and then measures the time it takes them to reach the detector. Kinetic energy is given to all analysed ions for short distances using the voltage difference. If the particles all have the same charge, the kinetic energies tends to be identical, and their velocities, in this case, will depend only on their masses. As a result, lighter ions will move at a higher speed. On a relatively long drift path, the elements are separated according to their masses. The individual elements are detected at different times as they hit the detector with multiplier. However, in reality, even particles with the same M/Z can arrive at different

times at the detector, because they have different initial velocities. In order to minimize these distribution errors, it is necessary to define the impact energy on the detector more precisely. This is accomplished by extending the distance the particle moves and using an electrostatic mirror. Importantly, the individual ion groups are separated from each other over time. Pulse beams are used for this purpose. The particles are removed from the surface by a precisely defined pulse of primary ions. Sufficient time delay prevents interference two consecutive groups of ions. By synchronizing the detector and the ion source, the flight time is measured accurately. The ability of the instrument to recognize ions of different mass is called mass resolution. It is defined as:

$$Res = \frac{M}{dM}, \tag{2.3}$$

where M is the average mass of the two signals that we observe, and dM their mass distance. Values slightly greater than 1 correspond to the nominal mass resolution (differentiation of signals distant by mass unit). Values in order of thousands corresponds to high-resolution (distinguishing signals that are distant by only a small mass fraction).

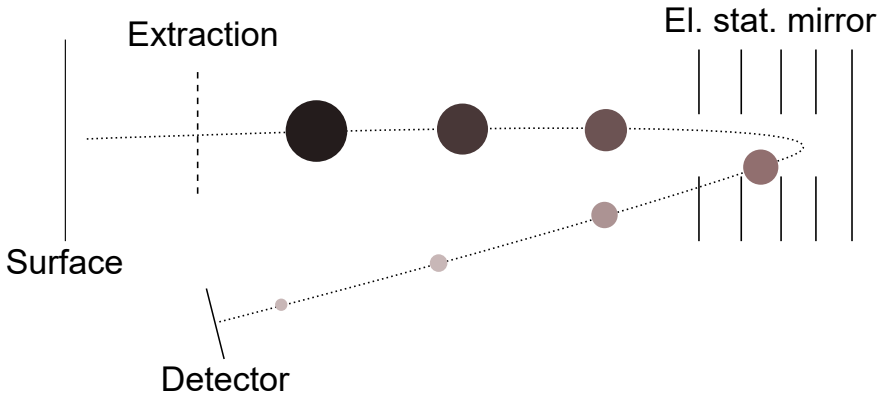

Figure 2.4: Schema of the mas-separation tube based on Time of Flight. Lighter ions impinge on the detector earlier than ions of greater mass.

2.3.2. Softwares

The data analysis software in ion beam methods are computer programs designed to extract information about samples from the measured ion beam spectra. The desired information includes the sample elements identification, concentrations and layer thicknesses. However, all this information can hardy be extracted from one single experiment. Number of codes were developed throughout the ages for the best interpretation of acquired spectra from various experiments. The software can also be used for designing relevant experiments. Depending on the assumed sample structure, the appropriate ion beam technique can be chosen by doing test simulations prior to experiments. The convenient choice of ions, energies, geometries, and so on can be examined.

SRIM/TRIM

Stopping and Range of Ions in Matter (SRIM) is a group of computer programs which calculate interaction of ions with matter; the core of SRIM is a program Transport of Ions in Matter (TRIM) calculating ion-solid interactions based on Monte Carlo method. The Monte Carlo method is an applied computer simulation of the decelerating and scattering

of energetic ions in materials. It has a number of distinct advantages over analytical formulations and allows for more rigorous treatment of elastic scattering and easy determination of energy and angular distributions [22]. Essential to this Monte Carlo method is its capacity of using randomness to solve problems that might be deterministic in principle. This approach is used for the binary collision approximation to select the next colliding atom [23]. Example of TRIM calculation of the maximal depth reached by proton penetrating the matter is shown in the Fig. 2.5.

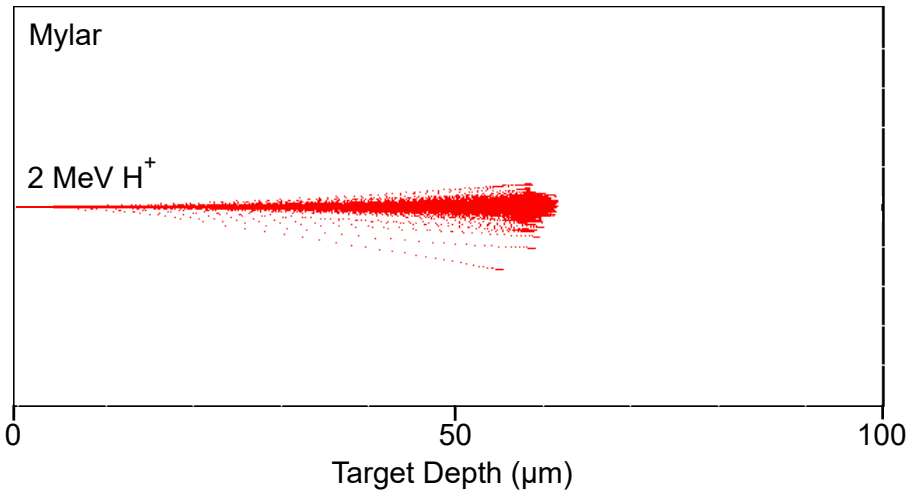

Figure 2.5: Depth range of 2 MeV protons in Mylar (C10-H8-O4) simulated by TRIM.

Part of the SRIM software allows for calculating the electronic stopping power of any ion in any material based on an averaging parametrization of a vast range of experimental data [6].

SIMNRA

SIMNRA is a program developed by Mayer [24] in 90's for the simulation of charged particle energy spectra for ion beam analysis with incident ions energies ranging from about 100 keV to many MeV. SIMNRA can be used for the simulation of both Rutherford Backscattering Spectrometry and Elastic Backscattering Spectrometry with non-Rutherford cross sections. In general, all IBA codes (except the Monte Carlo ones like in SRIM) employ similar principles to perform a basic simulation. The ingoing beam follows a straight trajectory, while losing energy, toward the sample. It interacts with a target nucleus and the outgoing beam follows a straight trajectory, while losing energy, on its way to the detector. Although all simulation codes treat basic ion stopping and scattering phenomena, many of the subtle features in backscattering spectra arise from more complex interactions.

The SIMNRA software uses the experimental details provided by the user to simulate a spectrum of scattered particles from the target. After loading the experimental data the initial conditions are based on the user's reasonable guess. Layers with any number of elements are created by defining the thickness and concentration values. The second step is to define the physics included in the calculation. The scattering cross sections are calculated using SigmaCalc [14]. These evaluated cross sections by the SigmaCalc code are based on a nuclear model and are in many cases more accurate than individual experimental data sets. The use of SigmaCalc cross section data therefore provides unsur-

passed accuracy for the simulation of elastic scattering measurements. Stopping powers are extracted from the SRIM-2013 stopping powers database [6]. SIMNRA also allows for including calculations for other physical phenomena like Bohr straggling and Andersen electron screening [25].

The target is divided into shallow sublayers. Each simulated spectrum is made up of the superimposed contributions from each isotope of each sublayer of the target. When the incident particles penetrate a sublayer, they lose energy due to electronic and nuclear energy loss and the beam energy is spread due to straggling. After accounting for these two processes, SIMNRA calculates the energy of backscattered particles from the front and the backside of the sublayer, and the energy of these particles which reach the detector after passing to the target surface. The contribution of each isotope in each sublayer is referred to as a brick. The brick area is determined from the mean reaction cross section in the sublayer, while its shape (i.e. the heights of the front and back edges) is determined from the cross sections at the entrance and exit of the sublayer and the change of the stopping power. The user can then iteratively refine the sample description until a good fit is reached or use a fitting routine to adjust the thickness and concentration of one layer at a time.

Multi-SIMNRA

The MultiSIMNRA software [26] uses multiple instances of the SIMNRA to calculate simulated spectra of different experimental conditions, and compares with experimental data using a χ^2 function (the sum of squared standard normal deviates). The fitting procedure is made by optimizing the χ^2 value modifying the fitting parameters accordingly to an optimization algorithm. It is considered that the final result represents the best possible match to the experimental data.

Potku

The software Potku (in Finnish *kick* or *recoil*) was developed as a user-friendly tool for heavy ion ERDA in 2014 [27]. The software uses as an input a list of measured coincident time of flight and energy (ToF–E) events (see Fig. 2.6). The ToF calibration can be determined with a simple graphical procedure. The graphical interface allows the user to select different elements and isotopes from a ToF–E histogram and to convert the selections to individual elemental energy and depth profiles. In Potku this is done by graphically placing polygons around the events in the ToF–E histogram belonging to each isotopic mass. The separation of every sample element in a ToF-ERDA measurement allows for determination of sample composition as a function of depth without any prior knowledge of the sample structure. In this iterative procedure the depth profile calculation is started by assuming a homogeneous sample composition obtained by correcting the total yield of each element with the corresponding scattering cross section. Stopping power for each recoil ion are then calculated for this initial sample composition, and the original depth for each detected recoiled or scattered particle is calculated backwards using the detected energy, stopping forces, and the known measurement geometry. The resulting depth distributions of the detected particles are again used to create a more accurate estimate of the sample composition and its stopping conditions. The calculation of the originating depths of particles and the stopping forces is repeated iteratively until the composition does not change significantly. When the sum of the individual elemen-

tal concentrations is scaled to the full 100 %, it becomes possible to integrate absolute concentrations over the depth of the thin film.

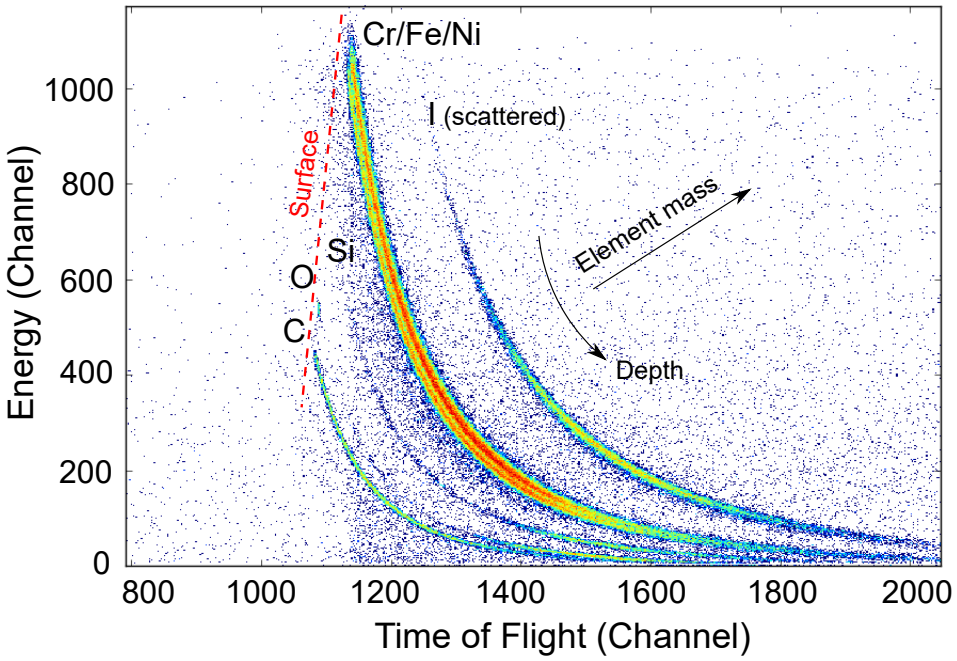

Figure 2.6: TOF-ERDA coincidence map obtained by bombarding C/Cr/Fe/Ni film on SiO_2 substrate with 36 MeV 127 I^{+8} beam. Each trace in the map corresponds to the different sample element as noted. Signals from near-mass heavy elements overlap in the map, whereas lighter elements are well separated. Red dashed line denotes the sample surface.

Gupix

The most suitable software package for the analysis of PIXE spectra is the GUPIX code [28] developed by the PIXE group at university of Guelph, Canada. The code allows for qualitative and quantitative analysis of X-ray characteristic lines in order to determine desired trace element concentrations in matrix, where major elements and their concentrations are known, but the GUPIX has also an extensive options for the more difficult problem of determining matrix composition i.e. major element concentrations in thick or layered unknown targets. With the good quality of the PIXE data base and by providing all aspects of the system (e.g. geometry, solid angle Ω, detector thickness and efficiency ξ, collected charge Q, filter absorption τ), peak areas could be converted to element concentrations:

$$C_Z = \frac{Y(Z,M)}{Y_T(Z,M) \cdot H \cdot Q \cdot \xi \cdot \tau}, \tag{2.4}$$

where the $Y(Z,M)$ is the X-ray intensity or yield for an element Z in a matrix M, $Y_T(Z,M)$ is the computed theoretical yield. Single quantity H describes the system. In a very well-characterized system H will be a constant representing the solid angle. In a not so well characterized system, H will be a function of X-ray energy and would require the measurement of standards.

The model spectrum is constructed using a data base of K, L and M X-ray energies, fluorescence probabilities and relative line intensities. Those are then modified to reflect the effects of detector efficiency, absorber effects and matrix effects. The matrix effects

in turn are computed using a data base of ionization cross sections and stopping powers, and X-ray mass attenuation coefficients. Ionization cross section are calculated based on ECPSSR [29] theory and optionally can be chosen from various experimental data [30]. The characteristic X-ray peaks are described by using a Gaussian line shape function, while the continuous background is effectively omitted from the spectrum by applying a simple digital filter designed to attenuate the low frequency spectral components (continuum) while passing the higher frequencies (peak structure). The intensities of the characteristic X-ray peaks are then determined by fitting the model spectrum to the measured spectrum using non linear least squares fitting technique.

In a layered case, it is assumed that each layer has uniform composition and thickness, that any given fit element can only be present in one specific layer, and the user is given the option of iterating the matrix composition (MCI) or thickness of each layer (LTI) to reach a 100 %. First, the spectrum is fitted as if it were a thin target - no thick target corrections are done for the relative line intensities. Once the initial estimates have been made, the iteration procedure begins.

2.4. Total IBA and self consistent approach

By the term *Total IBA* we refer to the benefits coming from combining the ion beam techniques to increase their individual power. The underlying idea of Total IBA is that with suitable instrumentation all ion beam-solid interaction products can be detected simultaneously, and the resulting information interpreted self-consistently. The comprehensive reviews on the current state of the Total IBA and its full potential was throughout last decade led by C. Jeynes [31–34]. For the purpose of this thesis only the brief introduction will be plotted to give an impression about the advantages of IBA and thus about the motivation for this work.

In the previous section, covering the ion beam techniques, we found that by changing the type of incident ion, geometry of experiment, particle energy, or by acquiring different products originating from ion and matter reaction, various information can be extracted. The fact that all product has the mutual origin in the one reaction defines the strong complementarity of the applied techniques. It means that if an integrated approach is used, where some combination of RBS/PIXE/EBS/ERDA is systematically done, then not only does the range of measurable samples but also the quality of information about each sample increases.

The desired goal for any thin film analysis was always the quantitative elemental depth profiling. While IBA has been used by analytical chemists for over half a century, in the 90's IBA methods were rather overtaken by rapid developments in other techniques. However, all have limitations and quantification was always an issue. Dramatic developments in IBA during the last decade, by growing stopping power database and accurate non-Rutherford cross section calculation, have made it significantly more powerful.

> "The strength of one technique is not properly recognised unless the limitations of the others are also understood" [31].

Standard methods for elemental depth profiling of thin films include Secondary Ion Mass Spectrometry (SIMS), Transmission Electron Microscopy (TEM) and X-ray Photoelectron Spectrometry (XPS). All of these have very well developed instrumentation and a large analytical literature with very wide applicability.

SIMS technique described is Sec. 2.2.5 has a very high sensitivity, but its problem is that the ionisation probability for secondary ions may vary by orders of magnitude; and the matrix effect is usually huge. This means that quantification is always difficult.

XPS spectra are obtained by irradiating a material with a beam of X-rays while simultaneously measuring the kinetic energy and number of electrons that escape from the top 10 nm of the material. XPS is therefore a surface sensitive technique. It uses high resolution electron energy analysers which allows for the detection of chemical shifts in the electron binding energies. The great advantage of the technique is the ability to distinguish between (for example) oxidation states. However, to use it for depth profiling, the sputtering of the sample is required when the X-ray spectra is acquired after each sputter increment.

TEM is an extraordinarily powerful technique, allowing atomic-level structural information by direct phase contrast imaging of atoms and also using selected area diffraction to identify the crystal structure. Elemental sensitivity can be obtained either by including an Energy Dispersive X-ray detector (EDX), or by using the energy-analysed transmitted electrons, so-called Electron Energy-Loss Spectrometry (EELS), where the information derives from the effect of target atomic excitation on the primary beam. However, TEM has a number of weaknesses. Sample has to be prepared in form of thin lamela which preparation is laborious, time consuming, and can be very difficult. Determining quantity of material is usually impossible because sample thickness (on which the EELS or EDX signals depend) is a strong function of the sample preparation, which is hard to control and very difficult to measure.

Various artefacts of sputtering which can be both large and rather intricate, especially in the presence of interfaces, are usually a strong function of the composition. The surface is also an important interface, which is tricky to analyse reliably by sputtering methods.

The strengths and capabilities of ion beam analysis (IBA), which uses an MeV ion beam to probe the sample is that there is no need for removing the material to probe deeper layers and thus quantification becomes possible. Among all the techniques mentioned above, RBS is distinctive since the interaction cross section is described analytically, the energy loss is rather insensitive to chemical effects and generally energy loss can be estimated for arbitrary materials following the Bragg's rule. Thanks to this RBS becomes a suitable primary reference technique with the best accuracy available for non-destructive model-free methods in thin films. Although it is known that RBS has severe limitation. The RBS method is rather ambiguous because of the systematic elemental overlaps. Kinematics and total resolution restrict the distinguishing of heavy close-mass elements and, moreover, any particular count could potentially originate from the scattering at heavy atom deep in the target, or at light element close to the surface. Nevertheless the mass overlap problem could be unambiguously solved with the addition of the PIXE data. Well resolved characteristic lines allows qualitatively describe sample structure and, in a well described system, quantitatively find elements with concentration at the level of millionth of a gram per gram (ppm). However, the PIXE by itself is blind to whether the films are 10, or 1, or 0.1 microns thick. It is only the simultaneous implementation of PIXE and RBS that can provide the depth profile of major and minor atomic constituents. The strength of the combination has been known for a long time and widely published [35–37].

However powerful the RBS/PIXE are, the light elements problem still remains unresolved. Efficiencies of X-ray detectors restrict the detection of characteristic lines from elements above sodium and kinematic and Rutherford cross section for light elements

curtail the RBS method sensitivity.

The (non-Rutherford) differential scattering cross sections, for most of the reactions with light elements, have been, during the last decade, measured and evaluated, to the extent that the analysis at sharp resonances effectively becomes tool for accurate depth profiling of light constituents as C, O, N.

Also the detection of the elastic recoils in ToF-ERDA has the great advantage that the mass overlaps can largely be avoided. The detected particles are recoiled from the sample; and can therefore, in principle, be sorted by mass. The great virtues of this technique is its high sensitivity to low-Z contaminants as well as their quantification. Moreover, the hydrogen as an element inaccessible to RBS, since nothing is backscatter from H, can be detected as a recoil. Total-IBA as a combination of RBS/PIXE/EBS/ERDA methods thus becomes a invincible weapon in the filed of thin film analysis as all limitations are largely overcome when the proper synergistic use of IBA methods is handled. Mutual (self-consistent) interpretation of each respective method, when the results from one technique becomes iteratively a boundary condition for the other, is massively more powerful than only any of the individual IBA techniques taken separately.

3. Experimental description

3.1. IBA setup at Tandem laboratory

3.1.1. The particle accelerator

The IBA measurements were carried out at the Tandem Laboratory at Uppsala University, Sweden. Four dedicated sources in combination with the 5 MV NECv5SDH 2 pelletron accelerator are capable of supplying a broad range of different light and heavy ion species with energies from 2 MeV to several ten MeVs. Such a variety enables for a number of different techniques including the ion beam analysis. Tandem accelerators locate the ion sources outside the terminal, which is at high voltage and usually placed inside a gas tank. Accessing the ion sources is thus significantly less difficult. Basically, in the first stage negative ions are produced and injected from a relatively lower voltage platform towards the high voltage terminal with a positive voltage V (millions of volts). Inside the terminal, the beam impinges on a thin metal foil, stripping electrons from the ions so that they become positive with multiple charge q. These ions are further accelerated while travelling to the bottom of the accelerating tube kept at the ground potential. As a result the ions emerging out of the accelerator gain energy $E = (q + 1)V$. The ions are bent by an analysing magnet through 90° depending on the mass, energy and charge state of the ion. The magnetic field of this magnet can be set to select the particular ion of required energy and charge state. Following magnet at the entrance to the analysis room then deflects the beam into one of the six beam lines dedicated for different ion beam techniques. There is a way of directly measuring the alpha particle beam energy (at 0.5 % accuracy) by means of using the well-established nuclear resonance $^{16}O(\alpha,\alpha_0)^{16}O$ at 3037 keV. Details on the employed energy calibration procedure for the primary beam can be found in details in [38].

3.1.2. Beam line

PIXE installation and following IBA experiments were performed in two different chambers along the 4th beam line. The full schema of T4 chambers is depicted in Fig. 3.1. Centres of both chambers occupy sample-holders mounted on goniometers, which are remote-controlled, enabling simultaneous data acquisition and sample movement. Sample holder in the first chamber is designed as a wheel with multiple target back-mounted at its outer edge. Up to 27 samples can be mounted to the holder within the windows of $\approx$ 10 mm in diameter. Goniometer allows for changing the sample by simple wheel rotation and also for wheel tilt around x, y axis to manipulate the beam-target angle. The first chamber features Passivated Implanted Planar Silicon (PIPS) type of solid state detector placed at $\vartheta = 170°$ scattering angle, with solid angle $\triangle\ \Omega = (2.16 \pm 0.11)$msr.

The PIPS detector used has a resolution of FWHM ≈ 13 keV for the whole detection chain and it's used for Rutherford Backscattering Spectroscopy, Elastic Backscattering Spectroscopy and particle-particle Nuclear Reaction Analysis (NRA). The first chamber also holds a telescope tube for Time of Flight-Energy coincidence Recoil Detection Analysis (see [39] for further details).

The second chamber is equipped with another telescope tube for ToF-ERDA measurements using an ionization gas detector chamber. The target holder has form of ladder which can accommodate 7 thin foil targets of 10 mm diameter. The goniometer remotely controls the movement along vertical direction as well at the rotation around z axis. The samples are mounted with the sample normal positioned under 67.5° with respect to the incident beam. The ToF-E telescope is fixed at 45° with respect to the direct beam. Two thin carbon foils placed in the telescope tube are separated by 425 mm. Further details on ToF-ERDA instrumentation at Uppsala University can be found in [40]. The detection efficiency in the ToF-detector, which differs from unity in particular for light recoil species, has been corrected in the analysis Potku code [41].

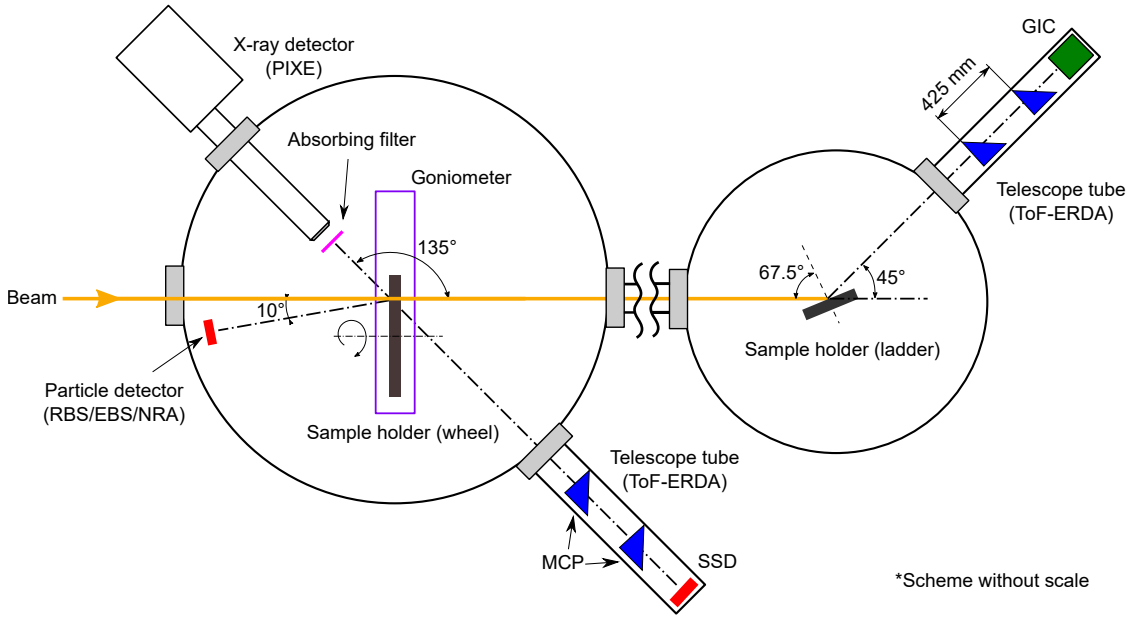

Figure 3.1: Detection setups of two vacuum chambers located on T4 beam line. In the first chamber the samples are mounted on the sample holder wheel fixed to the goniometer. The energy detectors for RBS, PIXE and ERDA are located at angles of 170°, 135° and 45°, respectively, with respect to the incidence direction. The second chamber feature another ToF-ERDA detection system at 45° and a ladder sample holder positioned in the grazing angle towards the incidence direction. The figure is not drawn to scale.

Each detection system, including also the carbon foils, require the external power supply unit. Bias applied to the detector through the BNC cable forms the voltage gradient attracting the product of radiation reaction with detector medium to create a pulse. At the end of the whole acquisition chain the spectra is formed. For the nuclear techniques the spectra show energy loss, and the interpretation of the spectrum depends on the spectrometer calibration. That must be done separately by the linearisation of the acquisition chain through the use of a proper model of the detector, which always has an entrance dead layer in which the particle loses some energy, with the energy loss being a function of the particle energy. Therefore, the detected pulse height is not a linear function

of the incident particle energy. This effect is known as the Pulse-Height Defect (PHD) non-linearity in keV per channel. Linearisation is usually done by scanning the beam between the samples with known composition certified as a standards.

The chamber is pumped in two stages by rotary pump and consequential turbo molecular pump to maintain a vacuum in the range of 10^{-7} mbar in the chamber and the beam line.

3.1.3. Data acquisition system

The transportation of the initial pulse into computer in accessible form requires the system of electronic devices namely preamplifier, amplifier and analog digital converter.

The basic function of a preamplifier is to amplify weak signal from a detector and to transport it through the cable that connects the preamplifier with the rest of the acquisition chain. At the same time, it should add the least amount of noise possible. Since the input signal at the preamplifier is generally weak, preamplifiers are mounted as close as possible to the detector. In this way, the undesired effects of the cable, mainly its capacitance, which decreases the signal-to-noise ratio, are minimised.

The amplifier, as the third block in the chain, already works with the signal enough intensive to be processed elsewhere. It usually serves to two main purposes; (I) Amplifies the signal from the preamplifier once more and (II) shapes it to a convenient form for further processing. In both cases, the amplifier must always preserve the information of interest. In contrary to the preamplifier the user has a full access to amplifier and to the pulse shaping. In general, the pulse coming from the preamplifier is characterised as an exponential with a long tail lasting anywhere from $10 - 100\,\mu$s. The amplitude of this pulse is proportional to energy. If a second signal arrives within the short period it will overlap with tail of the first and thus cause the distortion known as pile-up. To avoid this effect, either the counting rate has to be restricted to less 1 pulse period or the tail is shortened by reshaping into more advantageous Gaussian or triangular form. An adjustable gain over a wide range provides a scale adjustment of output spectra.

The output shaped pulses are in the final stage processed by Multi-Channel Analyzer (MCA) that consists of Analog-to-Digital Converter (ADC). The ADC converter measures the maximum amplitude of an analog pulse and converts that value to a digital number. The digital output is a proportional representation of the analog amplitude at the ADC input. For sequential arriving pulses, the digital outputs from the ADC are sorted into a histogram that corresponds to the energy spectrum observed by the associated detector.

3.2. PIXE detection

Particle Induced X-ray Emission (PIXE) is a highly sensitive, multi-elemental analytical technique which is already proven in all prospective areas such as thin films. This technique provides more accurate result for elemental analysis than others. Generally this technique is used to determine the elemental concentration of different elements dissolved in the samples. However, there was no complete PIXE setup at Uppsala University, Sweden. The aim of the practical part of this work is to introduce PIXE setup to T4 beam line at Tandem lab and to demonstrate its application for quantitative analysis on thin films.

3.2.1. Two detectors story

The ion beam facility at Uppsala university has been in former times extended to allow elemental concentrations analysis by PIXE. Two of Amptek Silicon Drift Detector type X-ray detectors were acquired to serve this purpose. However, the interest of the lab was redirected away from PIXE analysis and thus the detectors became forgotten for a while. Though, the advantages derivable from the PIXE analysis couldn't be overlooked indefinitely; and detector installation turned to be a needed improvement.

Both types XR-100SDD and X-123SDD feature the identical silicon drift detector described in Sec. 2.3.1. The active area of the detector is 25 mm^2 collimated by multilayer to 17 mm^2 with the thickness of the silicon crystal 500 µm. A polymer coated beryllium window (12.5 µm thick) is equipped with the detector to protect the active layer and to seal the atmosphere inside the detector tube. Direct cooling and pulse acquisition enhance the detectors counting performance and energy resolution. Detailed description of the system including all electronic and mechanical parameters can be found on-line at [42].

In the XR-100SDD, the detector is mounted on an extender (228.6 mm long and 17.78 mm in diameter), with the preamplifier in the attached metal box. For the full functionality it requires a separate signal processing and external power supplies. The X-123SDD providing, in a single package, the XR-100SDD detector and preamplifier; the Digital Pulse Processor (DPP) with pulse shaper, MCA, interface; and the Power Supply. All that is needed is a +5 Volts DC input and a USB connection to computer. Included software DPPMCA is a Windows application that provides data acquisition, display, and control for signal processors. It is worth mentioning that there is a different philosophy in the pulse processing. Standard procedure operates with the pulse in the analog form and digitalization takes place only at the end of the acquisition chain, whereas in X-123SDD the pulse is digitalized just after preamplifier. The possible addition of noise along the analog processing is thus minimised and moreover the digital pulse shaping brings some advantages over the analog shaping.

Even though it appears that X-123SDD is unbeatably more attractive for the PIXE installation than XR-100SDD, other aspects had to be considered. The whole laboratory detection system is connected through internal BNC network, which allows for transporting the signal from amplifiers to the MCA distant from chambers. Within one software signals from all detectors among the Tandem lab can be acquired, digitalized and displayed as spectra. Moreover, it allows for simultaneous signals acquisition from number of detectors, where the coincidence measurements or accurate derivation of collected charge play the crucial role in further analysis. Self standing software operating above X-123SDD would have to be additionally installed for PIXE spectra formation and simultaneous acquisition wouldn't be possible. For the given reasons the XR-100SDD was chosen as a better candidate for a PIXE system.

3.2.2. Power supply unit

Since the preapmlifier output of XR-100SDD has a simple BNC connector the signal can be processed in the standard way using the ORTEC 570 Amplifier. However, supplying the needed power to detector becomes rather challenging. Power supply input providing the bias to the detector and preamplifier is no more a simple BNC connector, as for the standard particle detectors, but more complex 6-pin LEMO connector. Function of each pin shows the Table 3.1.

Table 3.1: XR-100SDD 6-Pin LEMO Connector Pin Out [42]

Pin 1	Temperature monitor diode
Pin 2	Detector Bias, -100 to -180 V
Pin 3	−9 V Preamp. power
Pin 4	+9 V Preamp. power
Pin 5	Cooler power return
Pin 6	Cooler power 0 to +3.5 V *at* 450 mA
Case	Ground and shield

There is no commercial power supply unit suitable with XR-100SDD available on the market. Only the Amptek company offers a single compatible unit that includes desired power supplies but above that, also a Digital pulse shaping amplifier and an Integrated multichannel analyzer. Considering that only a power supplies would be used the price for the unit becomes unacceptably high.

The problem was solved by designing the new power supply box schematically shown in Fig. 3.2. The box serves as the BNC to 6-pin LEMO reduction from standard power supply unit where the additional power supplies for preamlifier and cooling are provided by electrical circuit. Bias applied to the detector can be thus easily tuned like in particle detector. The box is plugged into standard 230 V wall voltage socket.

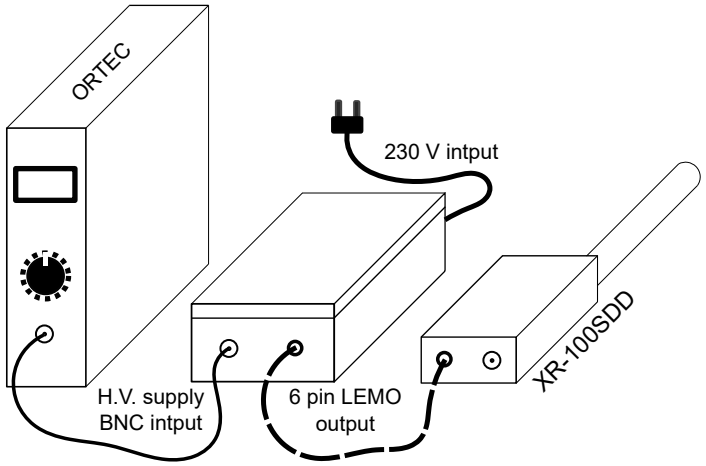

Figure 3.2: Schema of XR-100SDD power connection including the power supply unit box.

3.2.3. X-ray fluorescence setup

To prove the functionality of XR-100SDD in designed solution and compare its performance with X-123SDD, instead of complicated vacuum installation, the X-ray fluorescence (XRF) setup could be used. Mini-X X-Ray Tube System produces an energetic X-ray radiation collimated on the sample, where the reaction leads to the excitation of the target atoms electronic system. The subsequent de-excitation follows the hole filling principle where the energy conservation forces the radiation to be emitted. The product of XRF is the same characteristic radiation as for PIXE, but the experimental system is less complicated and can be used in ambient laboratory conditions (see [43] for more details).

Geometry of the experiment using both X-ray detectors and X-tube as a source is schematically shown in Fig. 3.3.

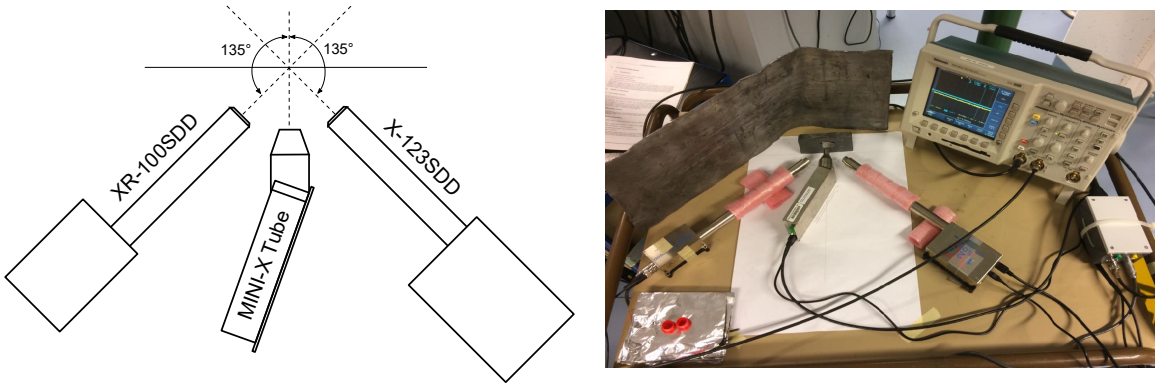

Figure 3.3: Left hand side: Sketch of the XRF setup geometry. Right hand side: Real experimental setup.

The internal setting for X-123SDD is done through the software interface and signal is directly displayed as a spectra. Connecting the XR-100SDD demands more attention, as for instance, applying the opposite bias polarity would irreversibly damage the detector. Following the Table 3.1 the detector requires the negative bias ranging from $-100\,\mathrm{V}$ to $-180\,\mathrm{V}$. Semiconductor device works as one-way valve for the current passing through the active volume. Characteristic of such device is the dark current flowing in the reverse direction known as a leakage current. Applied voltage over the junction can influence the amount of leakage up to the limit given by the power supply unit. High leakage current passing through the supply unit can damage the electrical circuit and is usually undesired. However, the present X-ray detectors are manufactured in the way that, to some extent, the leakage current is acceptable. Fig. 3.4 shows a dependence of leakage on the applied negative bias delivered by ORTEC power supply unit. Value $-115\,\mathrm{V}$ represents the highest stable bias where the leakage passing through the unit doesn't reach the safety limit.

Using the ORTEC 570 Amplifier, the pulses from XR-100SDD were amplified, shaped and then digitalized to create a characteristic spectrum. The best performance was obtained for amplifier setting: shaping time $10\,\mu\mathrm{s}$ and corse gain 500. MCA using 1024 channels digitalized the shaped peaks into final spectrum. It is worth noting here that there is an interesting philosophical difference between XRF/PIXE and RBS/EBS/ERD. The x axis units in particle energy spectra are the instrumental "channel number", where those for X-ray spectra are in absolute energy units (keV). This is because XRF/PIXE spectra show characteristic lines of the elements, where the line energies are natural constants: the calibration is determined by the spectrum.

Comparison of the characteristic spectra of the lead shielding acquired simultaneously by both XR-100SDD and X-123SDD is shown in Fig. 3.5. Comparably good quality of detector performance over exceed the initial expectation. XR-100SDD resolution of FWHM $\approx 136\,\mathrm{eV}$ for Fe^{K_α} measured on the coin is surprisingly high when differs from X-123SDD only by $\approx 8\,\mathrm{eV}$ (see Fig. 3.6).

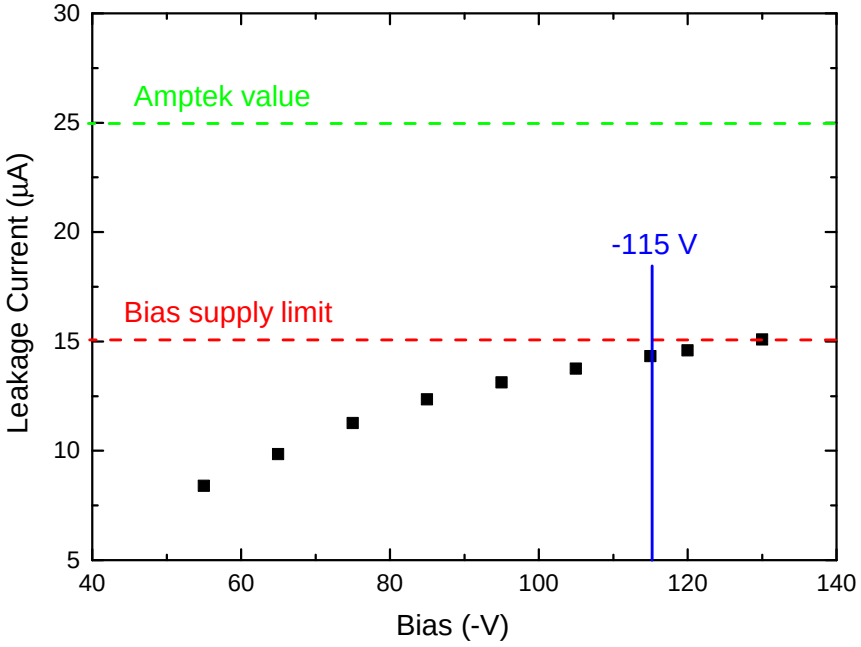

Figure 3.4: Dependence of the leakage current flowing through ORTEC supply unit on applied negative bias. Red dashed line at $\approx 15\,\mu A$ represents the supply unit limit. With Amptek's supply unit the leakage current can theoretically reach $\approx 25\,\mu A$.

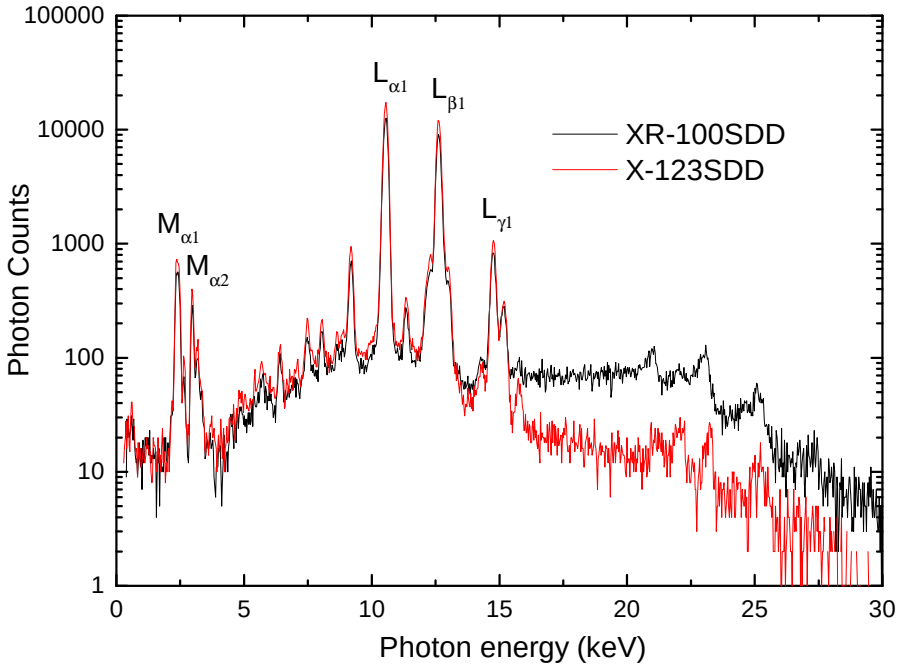

Figure 3.5: Comparison of characteristic X-ray spectra taken from lead shielding. Main M and L peaks are marked in the spectra. XR-100SDD shows slightly lower resolution and higher background in high energy region then X-123SDD.

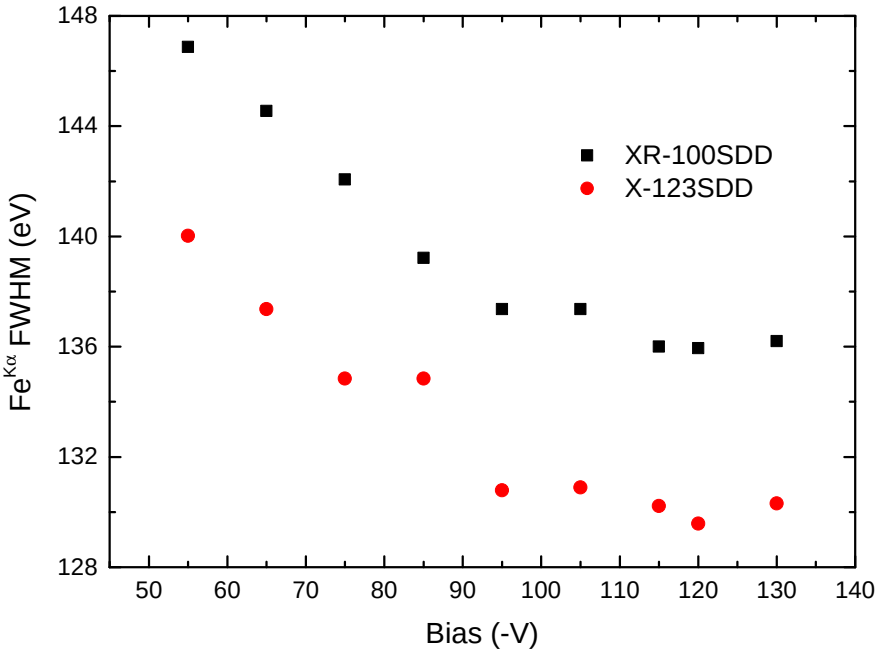

Figure 3.6: XR-100SDD and X-123SDD performance in dependence on applied bias. Trends are for voltage from -100 V reaching the constant values.

3.2.4. Vacuum chamber installation

After successful tests the XR-100SDD was installed into the first vacuum chamber at T4 beam line. The throughput port at 135° with respect to the beam was equipped by vacuum feedthrough connector ISO-KF 50 quick coupling flange. Vacuum in the chamber is then sealed by tightening the screw with an o-ring around the inserted detector extender. The closest distance between the edge of extender with detector and the sample was restricted by the goniometer construction. Rotatable goniometer arms occupy the centre of the chamber in the circle with diameter of ≈ 30 cm. To avoid the potential collision the detector was placed at a safe distance resulting in effective solid angle of $\triangle\Omega = = (1.875 \pm 0.056)$ msr.

3.2.5. Absorption filter

It was already briefly mentioned that the detector has to be protected from exposition of other products of ion beam-solid interaction. Detection of the energetically scattered ions and neutrals would prevent the detector from acquiring the X-ray radiation and could also damage the silicon crystal. Low Z elemental materials are used as a filters as their characteristic spectra lies under the detection limit and thus doesn't interfere with detected radiation. By the SRIM calculation of the ion stopping range in Mylar foil the minimum thickness was estimated to stop 2 MeV proton scattered of golden atom on the sample surface (see Fig. 2.5). A Mylar foil of 79.5 μm thick was fixed within a modified lid and placed in front of X-rays detector. Aside from stopping the ions it also acts as a filter to attenuate lower energy X-rays and to reduce X-rays interference. The role of the mass

attenuation for PIXE analysis can be found in [44]. Attenuation coefficients for materials used in this work are shown in Fig. 3.7.

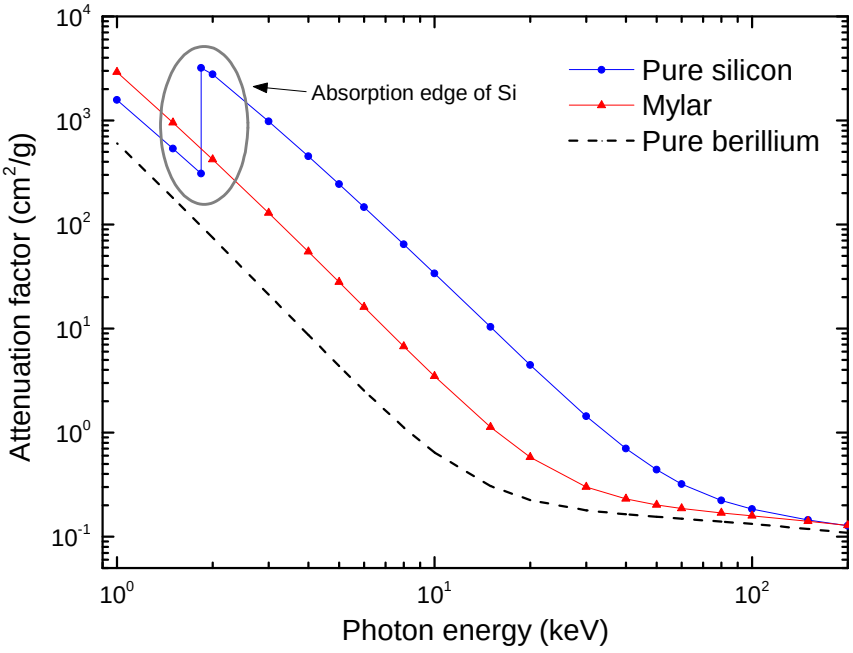

Figure 3.7: Mass attenuation coefficients for Be (black dotted line), Mylar (red), and silicon (blue) plotted on log-log axes. The absorption edge of silicon occurs around 1.74 keV. Simulated using XCOM database [45].

3.2.6. X-ray detector efficiency

Theoretical detector intrinsic efficiency is a function of detector parameters like thickness and density of detector crystal, contact layer and detector entrance window. It is crucial for the analysis to incorporate the detector efficiency. Fig. 3.8 shows the XR-100SDD efficiency as a function of X-ray energy. The curve was provided by the detector producer. Detection of low energy X-rays is mostly limited by the absorber filters (e.g. entrance Be window) and by absorption edge of the crystal (see Fig. 3.7), whereas high energy X-rays detection is limited by the size of the detection crystal. Sensitivity for light elements below sodium (1.04 keV) is almost zero.

Detector crystal nature leads to another artefact observable in the spectra. There is a $\approx 1\,\%$ probability that the radiation passing through the detector will excite the silicon electronic structure and hence lose appropriate amount of energy equal to the silicon K_α transition at 1.74 keV. Energetic characteristic peaks then have a satellite peak shifted by 1.74 keV towards the lower energies called escape peak.

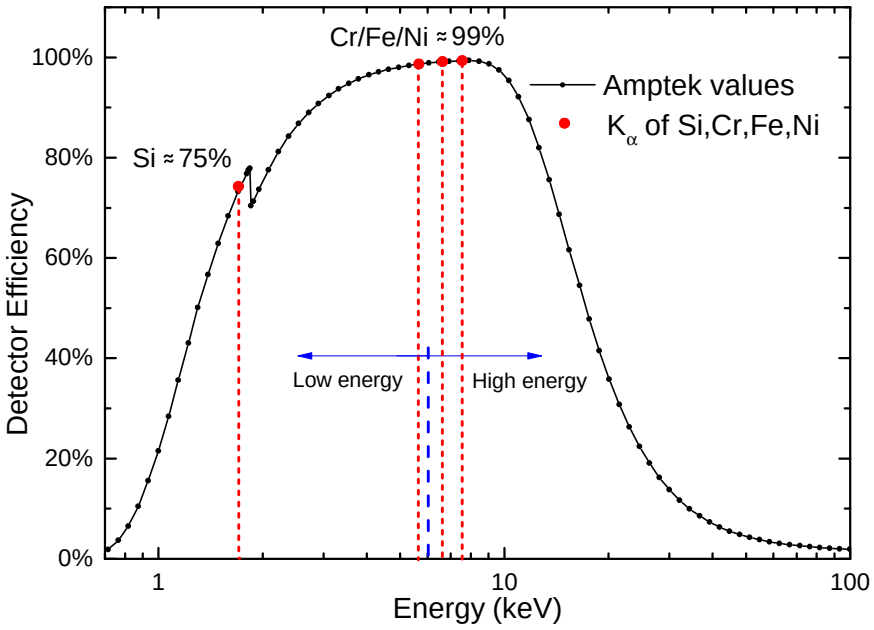

Figure 3.8: The intrinsic full energy detection efficiency for XR-100SDD. This efficiency corresponds to the probability that an X-ray will enter the front of the detector and deposit all of its energy inside the detector via electron-hole creation. Particular efficiencies for C/Cr/Fe/Ni/SiO_2 system are marked.

3.3. Total IBA

To demonstrate the powerfulness of ion beam methods with introduced PIXE, the system, rather difficult to be analysed without a X-ray detection, was chosen as a challenge. The series of ion beam based measurement of RBS, EBS, ERDA and in particular PIXE treated as a complementary techniques allowed for accurate elemental depth profiling of the studied system. Measurement and analysis performed within the scope of this work demonstrate a novel approach on utilization of ion beam techniques in such a wide range. Further work on the obtained data with precise treatment of the all kinds of uncertainties resulted into a manuscript recently recognized by scientific community. Preprint of the manuscript is attached to this thesis as an appendix.

The following section briefly introduces the problem and demonstrates my contribution to the publication.

Note: *The results, presented in the thesis, slightly differ from the ones in the paper. The new, updated version of the manuscript is currently under review.*

3.3.1. Anticorrosive alloys

For the present study, sputtered thin films of C, Fe, Cr and Ni were selected as a challenging model system. The motivation behind studying this particular material system is their

similarity to high-entropy alloys (HEAs), i.e., a new class of alloys that consists of four or more principal metallic elements at near-equimolar composition. The resulting alloys often exhibit rare combinations of useful properties, such as high strength and high resistance to corrosion. Due to the number of principal elements in a HEA, there is a unique opportunity to tune the material properties by adjusting the composition of the alloys [46, 47]. The system reduced into C/Cr/Fe/Ni was developed at Department of Chemistry at Uppsala University as a preliminary study of HEA's potential. The thin films were deposited in an ultra-high vacuum magnetron co-sputtering system, where the substrate was SiO_2 grown onto p-type Si(100) wafers. Fe, Ni, Cr and C-graphite targets with high purity were arranged around the substrate and by keeping the substrate holder still the compositional gradient in the films was created. Before depositing the films, a thin layer of Cr was deposited in order to increase the adhesion to the substrate. Since the trends in the material properties are related to the change in composition it is important to accurately determine the film composition at any point, especially the carbon content. For studying the corrosion resistivity it is also necessary to measure the amount of oxygen contamination in the films. The combination of several metallic elements with similar atomic numbers and the presence of C and O amounts make the quantification of the sample a true challenge. A $(1 \times 1)\,\mathrm{cm}^2$ piece from the center of the film was selected for ion beam analysis.

3.3.2. Ion beam analysis

As first RBS measurement was performed in the first chamber simultaneously with new installed PIXE. Thin film sample together with number of standards (i.e. pure gold, silver, silicon and copper) were mounted into sample holder wheel and attached to the goniometer. The 2 MeV He^+ primary beam delivered by the accelerator was then focused into $\approx 1\,\mathrm{mm}$ spot size using the Al_2O_3 target luminescence. The reason for using a He^+ instead of proton is simply the higher scattering cross section that ensures the broadening of energy spectra especially in expected heavy elemental overlap region, where the more details need to be observed.

The substrate formed by silicon dioxide may show crystallinity, thus the goniometer was programmed to wiggle (randomly change the incident/exit angles) the sample in small steps ($\pm 2^\circ$) around an equilibrium position in order to decrease possible channelling effects. For the same reason the RBS and PIXE measurements were not conducted in perpendicular position of sample surface and beam but for incidence and exit angles of 5° with respect to the surface normal. While this effect is not affecting the signals from the thin film directly, it would influence further PIXE quantification (discuses below).

The preliminary fitting of the RBS spectra by SIMNRA, applying the stopping power data from the most recent version of SRIM-2013 code, reveals that a good fit of acquired spectra, even with very limited prior knowledge, can be obtained. However, the correct stoichiometry of Cr, Fe and Ni is rather difficult to be unequivocally calculated as the signals from these species strongly overlap. In fact, discrepancies of several 10 % for the individual constituents are possible without affecting the fit quality.

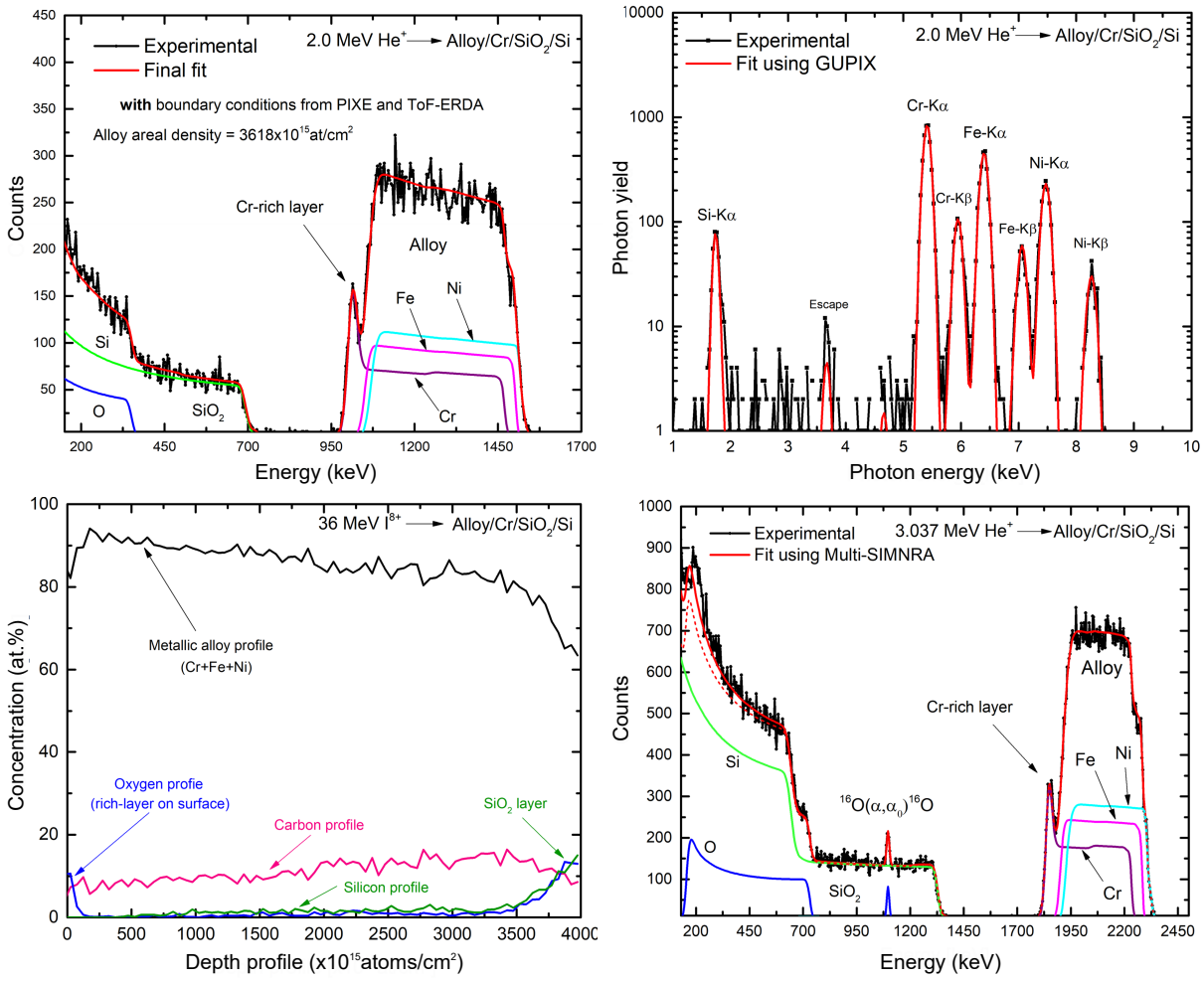

Figure 3.9: Left-upper corner: The black solid line represents the experimental RBS spectrum recorded for 2.0 MeV He^+ primary ions scattered from the alloy thin film. The red solid line represents the best fit provided by the SIMNRA code. Other color lines indicate the main constituents visible in the fitted spectrum. Data was evaluated with complementary input from PIXE/ToF-ERDA results. Right-upper corner: Experimental PIXE spectrum of the alloy sample (black dotted line) recorded together with RBS. The fit provided by the GUPIX code is also shown for comparison (red solid line). Left-bottom corner: Atomic concentration of the main constituents of the alloy as a function of their depth-profile deduced from the experimental ToF-ERDA spectrum using the Potku code. Right-bottom corner: Experimental EBS spectrum recorded at the resonance energy of 3.037 MeV, including the corresponding Multi-SIMNRA fit upon different energy spectra recorded during the EBS scan. Oxygen was detected only on the surface of the alloy.

It is now when, by observing the characteristic X-ray signals from the main metallic species present in the film, the powerfulness in RBS/PIXE complementarity is revealed. The characteristic peaks corresponding mainly to the K-shell emissions of the elements present in the alloy are well defined in the spectrum without overlaps. Pairs of K_α and K_β peaks for Cr, Fe and Ni are well separated and sorted with energy shift of ≈ 1 keV. PIXE thus enables quantification of near-mass elements with much higher accuracy than a fit of the RBS spectrum only. A signal from the Si/SiO_2 substrate can also be distinguished

as the characteristics X-ray have enough energy to not be fully attenuated in the metallic layer. Small observed escape peak than belongs to the most intensive Cr-K_α peak. Additionally, no evidence for heavy trace elements was found in PIXE spectra, indicating a clean sample preparation routine.

The peak areas, dependent on many instrumental parameters, are directly related to elemental abundance in the sample (see Eq. 2.4). Aiming to obtain the stoichiometry of the metallic elements present in the alloy with good accuracy, the GUPIX code was employed. To allow for the fit calculation a detail description of the experiment geometry and instrumentation, such as detection medium parameters, Be window thickness, the absorption filter and detector efficiency have to be considered in the GUPIX code. Charge Q collected during the ion exposure, required as an fit input, can be derived by two approaches. In the direct way, when the charge delivered by the beam is measured or in the indirect way, when the integrated charge is deduced from the $(particles \cdot \triangle\ \Omega)$ product derived during the RBS fit. In this work the indirect way appeared to be more suitable since the direct charge measurement features technical complication. Furthermore, the mass closeness of Cr, Fe and Ni ensures the identical detector's performance in their X-ray detection, so the instrumental value H could be conveniently kept constant as Ω. For the fit the sample structure was defined as Layer Thickness Interaction (LTI). Resulting stoichiometry was recursively employed in RBS fit as a boundary condition and thus more accurate RBS fit could be obtained.

In order to obtain absolute compositional depth profile the ToF-ERDA and EBS techniques were used to quantify the abundance of light elements (C, O, H) in the alloy. The ToF-ERDA measurements were done in the second chamber by delivering 36 MeV 127 I^{8+} ions as probe beam. There are two motivations for performing ToF-ERDA in the second chamber for the present study: at first, the ToF-E telescope is equipped with GIC detector, which doesn't suffer any damage under heavy ion bombardment. Second, the mass resolution for heavier components in the second system is typically found superior compared to the first system. ToF-E coincidence spectra were using well calibrated Potku code converted into depth profile. Note that the mass resolution for heavy and nearby elements (Cr, Fe and Ni) is relatively poor and their signals are overlapping. Nevertheless, the analysis allowed for carbon quantification throughout the film. No other light element were found in the alloy, except the small oxygen contamination close to the surface.

For an accurate oxygen depth-profile EBS measurement was conducted using the non-Rutherford $^{16}O(\alpha,\alpha_0)^{16}O$ resonance with a narrow shape (≈ 10 keV) at 3037 keV. The helium beam energy was modulated by small energy steps in order move the resonance peak deeper into the film. The resonance peak disappeared after the first energy increase, indicating the presence of only a very thin oxygen-rich layer on surface of the film.

By using all gathered information as a boundary condition for RBS fit the accurate alloy areal density 3618×10^{15} atoms/cm^2 could be derived. As final result from PIXE analysis, the total stoichiometry of the metallic elements in the sample were found to be Cr ≈ 31.8 at.%, Fe ≈ 33.5 at.% and Ni ≈ 34.7 at.%. A carbon concentration of ≈ 8 at.% close to the surface, slowly increasing up to≈ 14 at.% nearly its interface to SiO_2 layer was derived from ToF-ERDA. EBS additionally revealed small amount of oxygen contamination (9.23×10^{15} atoms/cm^2 ≈ 5 nm) present only at the sample surface, indicating high resistivity against corrosion. For the more information about the analysis follow the attached Paper I.

3.4. TOF.SIMS 5 instrument at CEITEC

The TOF.SIMS 5 is the latest generation of TOF-SIMS instruments developed over the last 25 years by IonToF company [48].

The basic instrument is equipped with a reflectron TOF analyser giving high secondary ion high mass resolution, a sample chamber with a 5-axis manipulator (x, y, z, rotation and tilt),electron flooding charge compensation, a secondary electron detector for SEM imaging, a state-of-the-art vacuum system, and an extensive computer package for automation and data handling. The most importantly, thanks to the modular design, the instruments is configured with a selection of optimised ion guns for various applications:

1. Duoplasmator, where the gas from reservoir is ionized by electron impact until the plasma is formed. Gun delivers up to 2 keV O_2^+ beam.

2. Surface Ionization source, where the Cs^+ ions are extracted by sublimation from solid alkali metal and ionized by contact with hot tungsten plate. Gun delivers 2 keV Cs^+ beam.

3. GCIB[1], where molecular ion clusters are formed by quick expansion of Ar^+ or $O_2{}^+$ gas and by consequential electron ionization. Cluster consisting of 5000 atoms can be formed.

4. LMIG[2], where the bismuth together with manganese are stored in a solid state. Sharp tungsten tip melts the solution and high energetic (2 keV) Bi_n^{+q} ions are ejected by extraction electrodes.

Ion guns feature a number of lenses, electrodes, beam pulsers and etc. to deliver a focused beam for the best measuring performance. The schema of TOF.SIMS 5 instrument is shown in Fig. 3.10.

Sources 1, 2 generate high-energy ions with the beam spot ranging from 30 µm to 50 µm, which are mainly used for coarse sputtering and crater creation. Implanted primary ions into the material also increase the overall yield either for positive or negative secondary ions. GCIB gun distributes the high impact energy among the cluster atoms and the induced surface damage is thus much lower. This source is conveniently used for analysis of organic samples, where the least molecular fragmentation is required.

The analysis of the crater bottom area is done with LMIG ion source. Several units of ns long pulses of focused Bi_n^{+q} beam (<100 nm) rasters the region of interest. Cycle time (pause between primary pulses, when the sputtered ions are analyzed) then determines the mass range in final spectra.

[1] Gas Cluster Ion Beam
[2] Liquid Metal Ion Gun

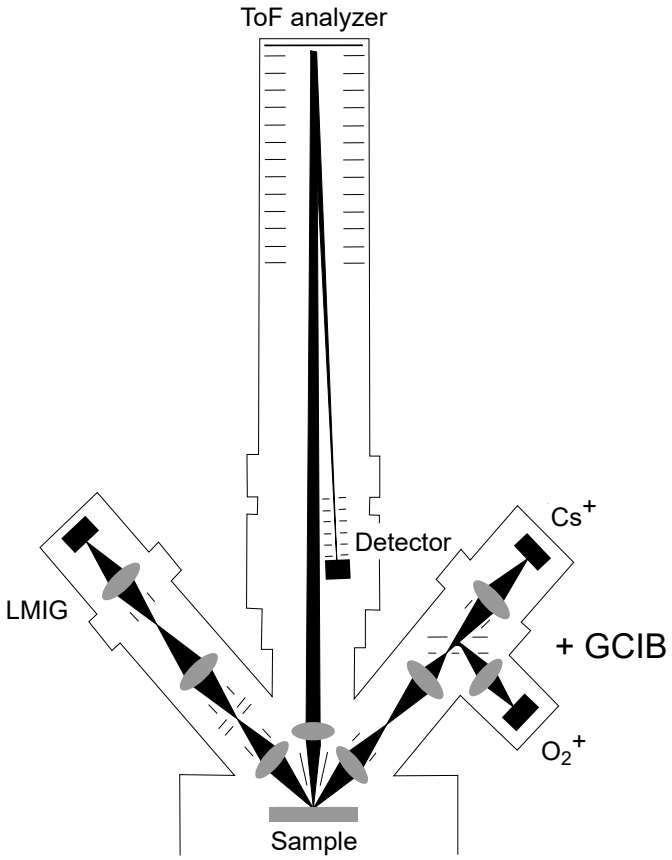

Figure 3.10: Schematic layout of TOF.SIMS 5. Adapted from [18].

The sputtered secondary ions are directed to the analyzer by applied electric field. The following ion mass separation is performed using the TOF method discussed in Section 2.3.1. The TOF.SIMS 5 uses a special secondary ion detector with a single channelplate-scintillator-photomultiplier combination. In addition to the MCP mentioned in Sec. 2.3.1 the multiplied electrons are in the next step converted into photons and signal is amplified.

Data output of every measurement can be converted into three formats:

- Mass spectrum
- Compositional depth profile
- 2D or 3D elemental distribution

Initial instrument setting predefines the resolution of each output. In general, the choice has to be made between spectrometry and resolution mode. By favouring the mass resolution, the lateral is lowered and vice versa.

3.5. SIMS depth profiling

The ability of the SIMS method to remove more atomic layers during the sputtering cycle gives the possibility to explore the material at different depths. The depth profile is a plot of the measured intensities of individual sputtered ions over the sputtering time. Obtained elemental depth profile features the high depth resolution (<10 nm) and extreme sensitivity for all elements.

The motivations for performing the SIMS measurement on the sample are two: At fists to simply compare the quantity of accessible information deduced from single ion beam based technique SIMS with the extensive analysis using MeV beam and self-consistent approach described above. The second motivation is to challenge SIMS quantification. It is not usually a case that we have a prior knowledge about sample's compositional depth profile. By observing the change in ion yields one can receive a useful insight to ionization processes accompanying the ion sputtering.

The greatest effect on ion yield is the ability of an atom to accept or deliver an electron, i.e., the ionization potential for positive ions, and the electron affinity for ions negatively charged. Since the ionization process is highly affected by close-surface condition it can be, to some extent, controlled by introduction of either electro-positive or electro-negative element. During the primary beam sputtering the O_2 and Cs ions are implanted and mixed with the sample material. Caesium is positioned at the very right of the periodic table, which means that it has one electron extra willing to donate. Sputtered sample atoms with the higher electron affinity will accept this electron and become negative ions. When using the oxygen gun, the O bonds mostly to metallic elements and after sputtering leads to the formation of positive ions by stealing their electrons.

Depth profiling measurements were conducted in high vacuum with a base pressure 10^{-9} mbar using the combination of LMIG and primary ion guns.

The first depth profile was analysed by 30 keV Bi_3^{++} in area of $(40 \times 40)\,\mu m^2$ placed within the $(200 \times 200)\,\mu m^2$ crater created by 2 keV O_2 gun (575 nA). Sputtered ions with positive polarity were extracted. Predefined spectrometry mode ensures the good mass resolution whereas the lateral resolution is not needed. Within the 40 µs cycle time, the ions up to mass 150 amu were collected. After each frame analysed by LMIG, another five were sputtered by O_2. No stop condition was set. Measurement was manually stopped when the probe depth reached the SiO_2 substrate.

A similar setup was used for the second depth profile sputtered by the 2 keV Cs gun (124 nA), where the sputtering cycle was set to remove ten frames instead of five. Ions with negative polarity were analysed. Both depth profiles of significant elements are shown in the Fig. 3.11.

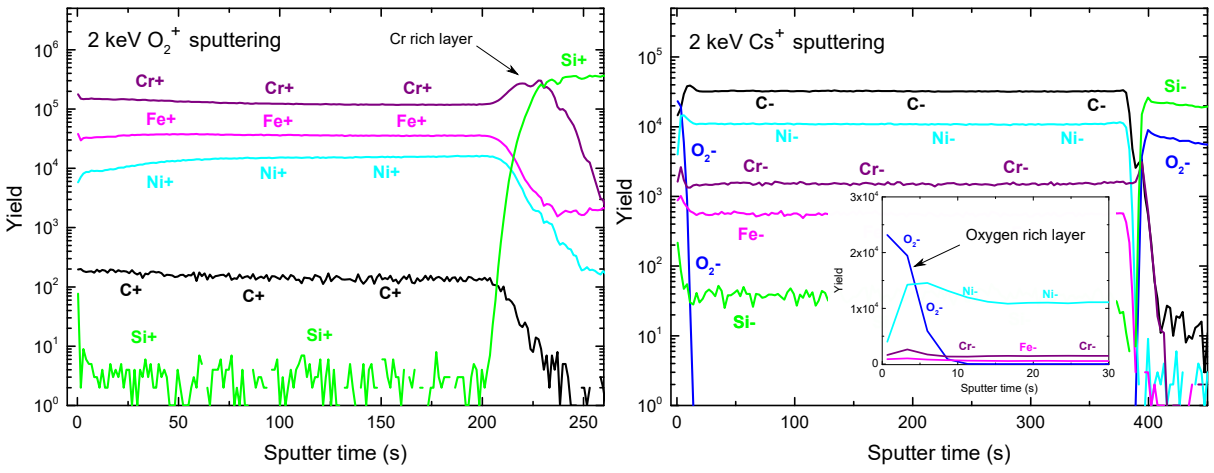

Figure 3.11: Left-hand side: Depth profile of the film sputtered by 2 keV O_2 gun when acquiring the positive ions. Right-hand side: Depth profile of the film sputtered by 2 keV Cs gun when acquiring the negative ions.

By observing the measured depth profiles one can easily notice the intensity order of main metallic constituents in the layer. It has to be clear that the order doesn't directly give the stoichiometry of Cr/Fe/Ni, instead, by applying the theory described above, it shows that the Cr can be more easily positively ionised than Fe and Ni thanks to the lowest ionization potential. On the other hand the Ni has the highest electron affinity and thus more easily accepts the electrons and becomes negative. The same applies for C, which rather forms a negative ion. Oxygen is included only in Cs sputtered profile, simply because there is no oxygen implanted, which would blur the information gained. In addition to the ionization process the sputter yield (probability that the target atom will be knock out) also differs for lighter elements. As a result there is not much to claim about the sample composition in terms of quantity.

Nevertheless, from a qualitative look we can learn more from SIMS then from each IBA technique separately. High depth and mass resolution allowed for distinguishing all alloy constituents and revealed their distribution in the sample. SIMS results are in the good agreement with IBA except for the carbon profile. All four main constituents (C/Cr/Fe/Ni) are according to SIMS homogeneously distributed throughout the film, whereas ERDA's depth profile (see Fig. 3.9) shows the small carbon gradient towards to surface. Observed gradient was in IBA confirmed by obtaining more accurate fit of RBS spectra when dividing the film in two areas with different abundance of carbon. However, SIMS analysis now rejects this observation, when revealing no carbon gradient behaviour in both measured depth profiles. Increasing plural and multiple scattering, with decreasing energy, affects the ERDA signals. This fact, together with the associated energy loss straggling may, in principle, have a deteriorating effect on the obtained depth profiles [49]. Results from SIMS are therefore more representative in terms of qualitative depth information then ERDA. This observation thus challenges IBA for further investigation.

The achieved depth is a function of the total sputtering time, sputtering conditions and sample matrix. In general, it is not easy to deduce the depth obtained. By using the complementary information about the depth from RBS the sputtering time can be converted into depth. The sputtering time around one or two seconds required to erode the surface oxygen layer would then correspond to $\approx 10 \times 10^{15}\,\mathrm{atoms/cm^2}$; in perfect agreement with EBS estimation.

Conclusion

The presented work emphasizes the utility of X-ray detection, enabling PIXE technique, which brings significant benefits into ion beam based analysis.

Convenient technical solution for X-ray detection with a state-of-the-art power supply unit, installed in T4 chamber at Tandem laboratory, allowed for simultaneous acquisition of RBS and PIXE with high resolution performance. The system, discerning all technical parameters like detector efficiency and filtering, was successfully tested and calibrated.

To demonstrate the strength and capability of Total-IBA, as a combination of the RBS/PIXE/EBS/ERDA methods, the complex alloy system containing metallic elements (Cr, Fe, Ni) as well as light elements (C, O) was elected as a challenge model. We qualitatively and quantitatively assessed the advantage of a combinatorial approach in order to obtain the complex chemical compositions of such materials. Self-consistent handling of experimental data evaluation resulted in accurate compositional depth profile of studied sample. The analysis revealed the film thickness, stoichiometry of metallic elements and abundance of light species, in particular the oxygen contamination on the surface. Based on this accurate determination of the film, the changes in composition can be related to material properties.

Further investigation of sample by SIMS method allowed for the study of ionization processes and above that challenged the results from ToF-ERDA. SIMS depth profiling qualitatively rejected the observed carbon gradient; and thus, opens opportunity for further investigation.

In conclusion, the thesis fulfils all its primary goals and moreover, part of the presented work, for its novel approach in self-consistent analysis, resulted in scientific publication.

References

1. Rutherford, E. The Structure of the Atom. *Philosophical Magazine* **27,** 488–498 (1914).
2. Nastasi, M., Hirvonen, J. & Mayer, J. W. *Ion-solid interactions: Fundamentals and applications* (Cambridge University Press, Cambridge, 1996).
3. Alford, T., Feldman, L. & Mayer, J. *Fundamentals of nanoscale film analysis* 1st ed. 336 pp. (Springer, London, 2007).
4. Chenakin, S. *et al.* Influence of screening and electronic stopping on LEIS spectra. *Nuclear Instruments and Methods in Physics Research B* **258,** 32–35 (2007).
5. Ziegler, J., Biersack, J. & Littmark, U. *The stopping and range of ions in solids* 1st ed. 321 pp. (Pergamon, New York, 1985).
6. Ziegler, J. *SRIM The stopping and range of ions in matter* `http://www.srim.org/` (2019).
7. Moro, M. *et al.* Stopping cross section of vanadium for H+ and He+ ions in a large energy interval deduced from backscattering spectra. *Nuclear Instruments and Methods in Physics Research B* **424,** 43–51 (2018).
8. Paul, H. & Sánchez-Parcerisa, D. A critical overview of recent stopping power programs for positive ions in solid elements. *Nuclear Instruments and Methods in Physics Research B* **312,** 110–117 (2013).
9. Sigmund, P. & Shinner, A. Electronic stopping in oxides beyond Bragg additivity. *Nuclear Instruments and Methods in Physics Research B* **425,** 110 (2018).
10. Wolf, B. *Handbook of Ion Sources* 1st ed. 560 pp. (CRC Press, 1995).
11. Tesmer, J. & Nastasi, M. *Handbook of Modern Ion Beam Materials Analysis* 1st ed. (Materials Research Society, Warrendale, 1995).
12. Bozoian, M., Hubbard, K. & Nastasi, M. Deviations from Rutherford-scattering cross sections. *Nuclear Instruments and Methods in Physics Research B* **51,** 311–319 (1990).
13. Gurbich, A. Evaluated differential cross-sections for IBA. *Nuclear Instruments and Methods in Physics Research B* **268,** 1703–1710 (2010).
14. *SIGMA calculation* `http://www-nds.iaea.org/sigmacalc/` (2019).
15. Leavitt, J. *et al. Nuclear Instruments and Methods in Physics Research B* **44,** 260 (1990).
16. Tesmer, J. *et al.* High energy and heavy ion beams in material analysis. *Materials Research Society* (1990).

17. Paul, H. K-shell ionization due to light ions: the status of cross-sections. *Nuclear Instruments and Methods in Physics Research B* **4,** 211–217 (1984).

18. Van de Heide, P. *Secondary Ion Mass Spectrometry: An Introduction to Principles and Practices* 384 pp. (John Wiley and Sons, 2014).

19. Gatti, E. & Rehak, P. Semiconductor drift chamber — An application of a novel charge transport scheme. *Nuclear Instruments and Methods in Physics Research* **225,** 608–614 (1984).

20. Lechner, P. *et al.* Silicon drift detectors for high resolution room temperature X-ray spectroscopy. *Nuclear Instruments and Methods in Physics Research A* **377,** 346–351 (1996).

21. Blum, W., Riegler, W. & Rolandi, L. *Particle Detection with Drift Chambers* 2nd ed. 448 pp. (Springer, 2008).

22. Biersack, J. & Haggmark, L. A Monte Carlo computer program for the transport of energetic ions in amorphous targets. *Nuclear Instruments and Methods in Physics Research* **174,** 257–269 (1980).

23. Robinson, M. & Torrens, I. Computer simulation of atomic-displacement cascades in solids in the binary-collision approximation. *Physical Review B* **9,** 5008–5024 (1974).

24. Mayer, M. *et al.* Computer simulation of ion beam analysis: Possibilities and limitations. *Nuclear Instruments and Methods in Physics Research B* **269,** 3006–3013 (2011).

25. Andersen, H. *et al.* Large-angle scattering of light ions in the weakly screened Rutherford region. *Physical Review A* **21,** 1891–1901 (1980).

26. Silva, T. *et al.* MultiSIMNRA: A computational tool for self-consistent ion beam analysis using SIMNRA. *Nuclear Instruments and Methods in Physics Research B* **371,** 86–89 (2016).

27. Arstila, K. *et al.* Potku - New analysis software for heavy ion elastic recoil detection analysis. *Nuclear Instruments and Methods in Physics Research B* **331,** 34–41 (2014).

28. Maxwell, J., Campbell, J. & Teesdale, W. The Guelph PIXE software package. *Nuclear Instruments and Methods in Physics Research B* **43,** 218–230 (1989).

29. Brandt, W. & Lapicki, G. Energy-loss effect in inner-shell Coulomb ionization by heavy charged particles. *Physical Review A* **23,** 1717–1729 (1981).

30. Campbell, J. *et al.* The Guelph PIXE software package III: Alternative proton database. *Nuclear Instruments and Methods in Physics Research B* **170,** 193–204 (2000).

31. Jeynes, C. & Colaux, J. Thin film depth profiling by ion beam analysis. *Analyst* **141,** 5944–5985 (2016).

32. Jeynes, C., Barradas, N. & Szilágyi, E. Accurate Determination of Quantity of Material in Thin Films by Rutherford Backscattering Spectrometry. *Analytical Chemistry* **84,** 6061–6069 (2012).

33. Jeynes, J. *et al.* Direct quantification of rare earth doped titania nanoparticles in individual human cells. *Nanotechnology* **27,** 285103–285111 (2016).

34. Jeynes, C. *et al.* "Total IBA" – Where are we? *Nuclear Instruments and Methods in Physics Research Section B* **271,** 107–118 (2012).

35. Bird, J. Total analysis by IBA. *Nuclear Instruments and Methods in Physics Research Section B* **45,** 516–518 (1990).

36. Landsberg, J., McDonald, B. & Watt, F. Absence of aluminum in neurotic plaque cores in Alzheimer's disease. *Nature* **360,** 65–68 (1992).

37. Silva, T. *et al.* Ion beam analysis of a-C:H films on alloy steel substrate. *Thin Solid Films* **545,** 171–175 (2013).

38. Paneta, V. *et al.* Accurate accelerator energy calibration using selected resonances in proton elastic scattering and in (p,c) and (p,p0c) reactions. *Nuclear Instruments and Methods in Physics Research Section B* **406,** 108–111 (2017).

39. Whitlow, H., Possnert, G. & Petersson, C. Quantitative mass and energy dispersive elastic recoil spectrometry: resolution and efficiency considerations. *Nuclear Instruments and Methods in Physics Research Section B* **27,** 448–457 (1987).

40. Ström, P. *et al.* A combined segmented anode gas ionization chamber and time-of-flight detector for heavy ion elastic recoil detection analysis. *Review of Scientific Instruments* **87,** 103303–103308 (2016).

41. Zhang, Y. *et al.* Detection efficiency of time-of-flight energy elastic recoil detection analysis systems. *Nuclear Instruments and Methods in Physics Research Section B* **149,** 477–489 (1999).

42. *AMPTEK* `http://amptek.com/` (2019).

43. Lekki, J., Matosz, M. & Paluszkiewicz, C. Comparison of PIXE and XRF in the analysis of silver denarii of the early Piast. *Journal of Radioanalytical and Nuclear Chemistry* **314,** 2309–2316 (2017).

44. Flannigan, E., Heirwegh, C. & Campbell, J. Role of the mass attenuation coefficient database in standardization of a silicon drift X-ray detector for PIXE analysis. *X-Ray Spectrometry* **47,** 63–71 (2018).

45. *XCOM database* `https://www.nist.gov/` (2019).

46. Yeh, J. *et al.* Nanostructured high-entropy alloys with multiple principal elements: novel alloy design concepts and outcomes. *Advanced Engineering Materials* **6,** 299–303 (2004).

47. Ye, Y. *et al.* High-entropy alloy: challenges and prospects. *Materials Today* **19,** 349–362 (2015).

48. *ION-TOF: Superior Performance for all SIMS Applications* `https://www.iontof.com` (2019).

49. Kantre, K., Paneta, V. & Primetzhofer, D. Investigation of the energy loss of I in Au at energies below the Bragg peak. *Nuclear Instruments and Methods in Physics Research Section B* **(Article in press)** (2018).

50. Campbell, J. *et al.* The Guelph PIXE software package IV. *Nuclear Instruments and Methods in Physics Research B* **268,** 3356–3363 (2010).

Paper I

Moro, M.V., Holeňák, R., Zendejas Medina, L., Jansson, U. & Primetzhofer, D. Accurate high-resolution depth profiling of magnetron sputtered transition metal alloy films containing light species: A multi-method approach. *arXiv preprint arXiv:1812.10340* (2018).

Accurate high-resolution depth profiling of magnetron sputtered transition metal alloy films containing light species: A multi-method approach

M. V. Moro[1, a], R. Holeňák[1, 2], L. Zendejas Medina[3], U. Jansson[3] and D. Primetzhofer[1]

[1]Department of Physics and Astronomy, Uppsala University, Box 516, S-751 20 Uppsala, Sweden
[2]Department of Physical Engineering, Brno University of Technology, 616 69, Brno, Czech Republic
[3]Department of Chemistry, Uppsala University, Box 538, S-751 20 Uppsala, Sweden

Abstract

We present an assessment of a multi-method approach based on ion beam analysis to obtain high-resolution depth profiles of the total chemical composition of complex alloy systems. As a model system we employ an alloy based on several transition metals and containing light species. Samples have been investigated by a number of different ion-based techniques, i.e., Rutherford Backscattering Spectrometry, Particle-Induced X-ray Emission, Elastic Backscattering Spectrometry and Time-of-Flight/Energy Elastic Recoil Detection Analysis. Sets of spectra obtained from these different techniques were analyzed both independently and following an iterative and self-consistent approach yielding a more accurate depth profile of the sample, including both metallic heavy constituents (Cr, Fe and Ni) as well as the rather reactive light species (C, O) in the alloy. A comparison in terms of achievable precision and accuracy is made and the limitations of the single method approach are discussed for the different techniques. The improved accurate information on stoichiometry, depth distribution, and thickness of the alloy from the multi-method approach can be correlated to the material properties such as superior corrosion strength of the alloy.

Keywords

High-resolution; composition depth profiling; Ion Beam Analysis; metal alloys; Magnetron Sputtered thin-films

[a] Corresponding author:
marcos.moro@physics.uu.se

1. Introduction

Ion beam-based analytical techniques represent a powerful set of tools for non-destructive, standard-less, depth-resolved and highly accurate elemental composition analysis in the depth regime from several nm up to few µm [1]. By changing type of incident ion, the geometry of experiment, particle energy, or by acquiring different products originating from ion-solid interaction, complementary information can be extracted. However, analysis is often challenged either in terms of mass resolution - when several comparably heavy elements are present in the sample - or in terms of sensitivity - when light species are present in heavy matrixes.

Hence, typically only a combination of several ion beam-based techniques will overcome the limitations of each individual method and provides complementary information about the sample. The most commonly employed ion beam analysis (IBA) technique is Rutherford Backscattering Spectrometry (RBS) [2], where light primary charged particles (typically H^+, D^+, $He^{+,++}$ and Li^+), detected after being elastically backscattered from target nuclei and inelastically decelerated by the electronic system of the target, are used for determining concentration profiles of the target constituents. The high accuracy of the method as well as high sensitivity has made it a common tool to characterize thin film deposition processes [3] or the effects of ion implantation [4]. Even though the accuracy of Rutherford scattering cross sections is much better than 99 %, limitations of RBS are found in, e.g., limited detector energy resolution, i.e., the inability to uniquely identify constituents with small relative mass differences due to similar scattering kinematics [5].

Additionally, the sensitivity for light constituents in heavy matrices is rather limited. Apart from backscattered particles, one may also detect other products of elastic nuclear collisions, i.e., recoiling target species. Time-of-Flight/Energy coincidence measurements of Elastically Recoiled target particles due to irradiation with heavy primary ions with several tens MeV's (ToF-E ERDA) [6] enables mass-resolved composition depth profiling without masking of the signals of light constituents, and with almost equal sensitivity for all constituents. The method is thus very suitable to quantify e.g. light electrolytes [7] or simply the concentration levels of undesired impurities [8]. Elastic Backscattering Spectrometry (EBS) [9] can also obtain complementary isotope-resolved information on light target constituents. This method is based on using elevated energies and employing resonant non-Rutherford cross sections, making use of the fact that interaction is no longer purely Coulomb between point charges. This phenomenon can enhance the probability to detect backscattered particles by orders of magnitudes with respect to expectations from Rutherford cross section. Finally, X-ray detectors allow for detecting the characteristic x-ray emission due to de-excitation of the target electronic system after passage of an ion. Particle Induced X-ray Emission spectroscopy (PIXE) [10] can be used to determine

the elemental concentration of nearby elements providing in parallel a signal even for trace impurities of heavier elements in the sample [11]. The latter property is due to the fact that Bremsstrahlung is effectively suppressed in comparison to electron-based x-ray excitation techniques.

As mentioned above, a combination of these techniques may be beneficial when the samples of interest contain light species in a heavy matrix, and strong gradients in concentrations may be expected. Assessing the advantage of such a combinatorial approach is of particular relevance since such complex chemical compositions are nowadays getting more abundant in many of the high-tech coatings employed today in mechanically or chemically challenging environments.

In this work, we present an iterative and self-consistent IBA analysis of carbon-containing transition metal alloys with light contaminants with a twofold goal. We critically assess the self-consistent approach adopted in this study, which combines different ion beam-based methods by simultaneously fitting experimental data where information obtained from each technique is used as a boundary condition for another. We compare the achieved accuracy to the ones obtained by the individual methods. In parallel, we show that a highly accurate full description even of complex samples of interest can be provided, which can yield improved understanding of the material properties and sample preparation pathways.

For the present study, sputtered thin films of C, Fe, Cr and Ni were selected as a challenging model system. The motivation behind studying this particular material system is their similarity to high-entropy alloys (HEAs), i.e., a new class of alloys that consist of four or more principal metallic elements at near-equimolar composition [12]. The resulting alloys often exhibit rare combinations of useful properties, such as high strength and high resistance to corrosion [13]. Due to the number of principal elements in a HEA, there is a unique opportunity to tune the material properties by adjusting the composition of the alloys [14].

To use this combinatorial method, the composition at any point in the films must be accurately determined, especially the carbon content. It is also necessary to measure the amount of oxygen contamination in the films. The combination of several metallic elements with similar atomic numbers and the presence of C and O amounts makes the quantification of the sample a true challenge.

2. Experimental procedure

2.1 Sample Preparation

The thin films were deposited in a home-built ultra-high vacuum magnetron co-sputtering system with a base pressure of 10^{-9} mbar at 300 °C. Argon gas at $4x10^{-3}$mbar was used to ignite the plasma and the substrate was SiO_2 grown onto p-type Si (100) wafers. Fe, Ni, Cr and C-graphite targets (purity ≥ 99.95%) were arranged around the substrate at an angle of 39° with respect to surface normal of the substrate (see Fig. 1, panel a). The graphite target was powered by a pulsed DC source with a frequency of 100 Hz, while the remaining targets used separate, non-pulsed DC sources. The substrate holder was not rotated, thus creating a compositional gradient in the films. Before depositing the films, a thin layer of Cr was deposited in order to increase the adhesion to the substrate (see Fig. 1, panel b). Following deposition, a 1x1 cm^2 piece from the center of the film was selected for ion beam analysis. The composition and thickness of the layers are discussed in details in Sec. 3.

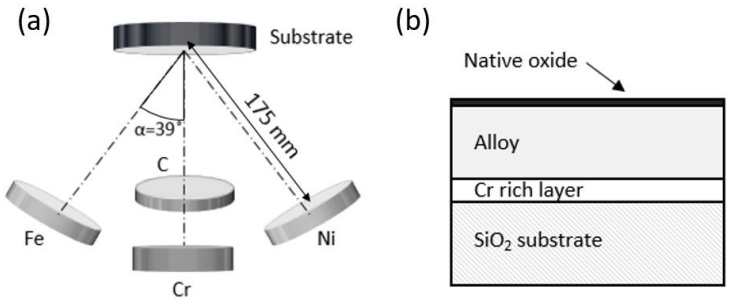

Figure 1. (a) Schematic illustration of the sputter chamber geometry: the four targets are positioned relative to the substrate. (b) Schematic cross-section of the sample, with the layers that are expected to be observed. The thickness of the layers is not to scale.

2.2 Accelerator and scattering chamber

The IBA measurements were carried out at the Tandem Laboratory at Uppsala University, using a 5-MV NEC-5SDH-2 tandem accelerator. Experiments were performed in two different chambers allowing for different techniques. The first chamber features passivated implanted planar silicon (PIPS) detectors for Rutherford Backscattering Spectroscopy (RBS), Elastic Backscattering Spectroscopy (EBS) and particle-particle Nuclear Reaction Analysis (NRA) and a silicon drift detector (SDD) for Particle-Induced X-Ray Emission (PIXE). It also holds a telescope tube for Time-of-Flight/Energy coincidence Recoil Detection Analysis (ToF-E ERDA) (see Ref. [15] for further details). The second chamber is equipped with another telescope tube for ToF-E ERDA measurements using an ionization gas chamber (GIC) (discussed below) as an energy detector as well as additional solid-state detectors for other IBA techniques. Both chambers feature sample-holders mounted on goniometers, which are remote-controlled, enabling simultaneous data acquisition and sample movement.

In the present study, RBS, EBS and PIXE measurements were performed in the first chamber, while ToF-E ERDA analysis was conducted in the second one. There are two motivations for performing ToF-E ERDA in the second chamber for the present study: at first, when heavy elements are present, the GIC does not suffer from radiation damage due to heavy recoils and scattered primaries to the same extend as a solid-state detector. Second, the mass resolution for heavier components in the second system is typically found superior compared to the first system.

2.3 Ion beam analysis

RBS measurements were performed using 2 MeV He^+ primary ions. Since the thin film was deposited onto silicon dioxide, which may show crystallinity, (e.g. in the form of texture), the goniometer was programed to randomly change the incident/exit angles of the sample in small steps (± 2°) around an equilibrium position along the measurements in order to decrease possible effects from residual channeling. Despite this effect is not affecting the signals from the thin film directly, it would influence the quantification of the charge-solid angle product from the substrate signal which can be helpful in the analysis. The PIPS detector used has a resolution of FWHM ≈ 13 keV for the whole detection chain, and it is placed at $\theta = 170^{o}$ scattering angle, with solid angle $\Delta\Omega = (2.16 \pm 0.11)$ msr. RBS measurements were carried out simultaneously with PIXE, and the total charge collection (needed for more quantitative PIXE analysis) was deduced by fitting the substrate signal in the RBS spectrum. The uncertainties involved in these measurements are discussed in details in Sec. 3.2.

EBS measurements were carried out using the elastic $^{16}O(\alpha,\alpha_0)^{16}O$ resonance at 3.037 MeV He^+ energy, which features a scattering cross section ≈ 35 times higher than the Rutherford value [16, 17]. Since EBS spectra can be very sensitive to the specific beam energy, one can scan the projectile energy in order to depth-profile the oxygen concentration into the film [18]. For an accurate oxygen depth-profile using EBS, the accelerator beam energy was beforehand calibrated, and the beam energy is known better than 0.5%. Details on the employed energy calibration procedure for the primary beam can be found in details in Ref. [19].

ToF-ERDA enables depth-profiling the elemental composition of thin films in a depth range of ≈ 1 µm, within a depth resolution of ≈ 30 nm close to the surface. The mass-separation of the recoiled ion species is accomplished by measuring their time-of-flight and energy in coincidence (ToF-E). In this work, the ToF-ERDA measurements were done by delivering 36 MeV $^{127}I^{8+}$ ions as probe beam and using the ToF-E telescope tube mounted in the second chamber at the fourth beam-line of the Tandem accelerator. The samples were mounted with the sample normal positioned under 67.5^{o} with respect to the incident beam. The ToF-E telescope is fixed at 45^{o} with respect to the direct beam. Further details on ToF-E ERDA instrumentation at Uppsala University can be found in [20]. The detection efficiency in

the ToF-detector - which differs from unity in particular for light recoil species - has been corrected in the analysis code [21].

For PIXE, x-rays are detected by a 500 µm thick silicon drift detector (SDD) placed at θ = 135° with respect to the primary beam. The x-ray SDD has a resolution of FWHM ≈ 136 eV for Fe-K_α characteristic energy, and a solid angle of ΔΩ = (1.875 ± 0.056) msr. A 79.5 µm Mylar absorber is placed in front of the 12.5 µm Be-window of the SDD to attenuate the low-energy characteristic x-rays (e.g., from Si) and Bremsstrahlung in order to decrease the dead time of the detecting system and to protect the detector from radiation damage due to backscattered particles.

3. Results and discussions

3.1. Iterative self-consistent characterization

In Fig. 2, we show an experimental RBS spectrum (black solid line) recorded for incidence and exit angles of 5° with respect to the surface normal. The figure also holds different fits obtained using the latest version of SIMNRA [22] (red line in panel (a) and (b) - other colors for constituents). The stopping power data used in all the fits presented in this paper was retrieved from the most recent version of SRIM-2013 code [23]. As apparent from the fits to the experimental RBS data in Fig. 2, a broad signal with extended plateau starting at the highest energies corresponds to ions backscattered from the metallic alloy constituents (Ni-Fe-Cr).

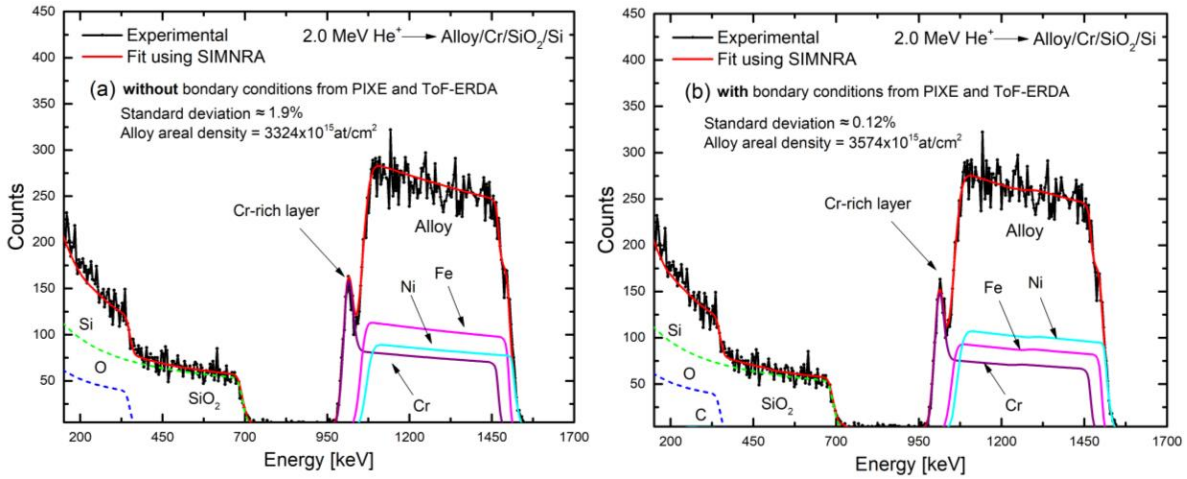

Figure 2. (Color online) The black solid line represents the experimental RBS spectrum recorded for 2.0 MeV He^+ primary ions scattered from the alloy thin film, as described in the Sec. 2. The red solid line represents the best fit provided by the SIMNRA code. Other color lines indicate the main constituents visible in the fitted spectrum. In (a), data were evaluated without further complementary input from PIXE nor ToF-ERDA results, whereas in (b), information from these techniques was used as boundary condition to the fit (see text for details).

For the fit shown in Fig. 2 (a), we did not assume any previous knowledge regarding the sample besides the alloy constituents (Cr, Fe and Ni) plus other elements visible in the spectrum (Si and O). Therefore,

the fit was obtained by changing composition and thickness iteratively until convergence is obtained (by minimizing the integral values of the difference simulation-experiment in the region [450 - 1700] keV in both spectra). As boundary condition for the input in fit presented in Fig. 2 (b), we used information obtained from other techniques, e.g., stoichiometry of Cr, Fe and Ni from PIXE, and carbon amount from ToF-ERDA (discussed in details below). Hence, the thickness of the carbon-containing alloy layer was the only parameter kept free to be adjusted by the fit.

As a result from the evaluation presented in Figure 2, the mean standard deviation between the fit – experimental data integrated in energy region [450 - 1700] keV was found to be 1.9 % and 0.12 % for the experimental and simulated spectra shown in panel (a) and (b), respectively. Although it becomes apparent that a reasonable good fit can be obtained in both situations, even if in the case where RBS fit is very limited with a-priori knowledge on the sample, the total areal thickness of the alloy can be deviating from the accurate value by around 7 %. Note that the integral areal density of the metal components, however, is obtained with higher accuracy. At the same time, the accurate stoichiometry of Cr, Fe and Ni is rather difficult to be derived directly from the RBS fit, as the signals from these species strongly overlap. In fact, discrepancies of several 10% for the individual constituents are possible without affecting the fit quality beyond the above mentioned 1.9%. Moreover, the amount of carbon – virtually invisible in the spectrum – needs to be considered during the fit to properly estimate the energy loss of the ion in the alloy layer.

While this result shows the expected advantage of employing multiple techniques putting constraints in the evaluation [24], it also shows the necessity of a quantitative evaluation of the fit quality. The observed differences in thickness and concentrations between the models employed in Figs 2a and b are far larger than the observed difference between fit and experiment. The result of the multi-method procedure shown in Fig. 2 (b) is quantitatively much better than the one in (a) (compare both chi-square values shown in the panels). Thus, from the iterative procedure total areal thickness of 3574×10^{15} at/cm^2, as well as a thin Cr-enriched layer of 120×10^{15} at/cm^2 ≈ 14 nm at the interface between the alloy and the SiO_2 layers could be unequivocally obtained with high accuracy (residual uncertainties are discussed in Sec. 3.2).

Similar improvements in deduced data, with almost identical fit quality are also observed for the other techniques. In Fig 3, the experimental PIXE spectrum (black solid line) as well as the corresponding fit using the GUPIX code [25] (red solid line) are shown. The characteristic X-ray signals originating from the main metallic species present in the film are the dominant structures in both experimental and fitted data (Cr, Fe, and Ni). A signal from the Si substrate can also be distinguished. The peaks corresponding mainly to the K-shell emissions of the elements present in the alloy are well defined in

the spectrum without overlaps. This data enables quantification of near-mass elements with much higher accuracy than a fit to the RBS spectrum exclusively. Additionally, by analyzing the main peaks present in Fig. 3, one can notice no evidence for heavy trace elements (Z >11 in the sample) within a quantification limit of better than 0.1 at.%, indicating a clean sample preparation routine.

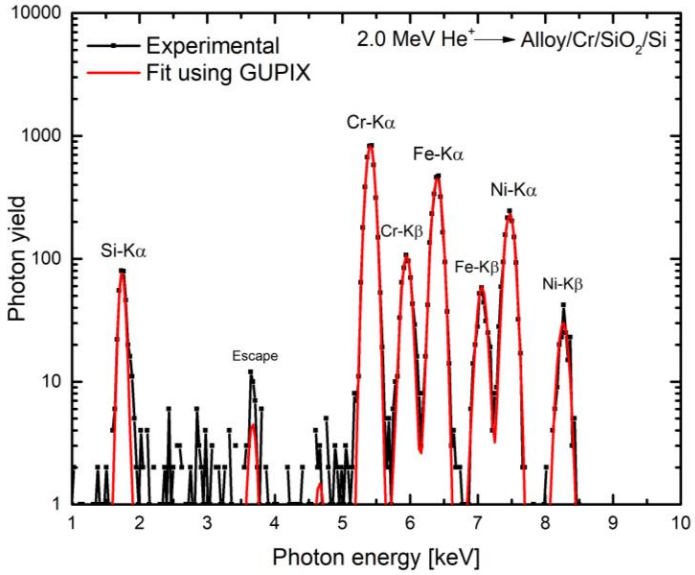

Figure 3. (Color online) Experimental PIXE spectrum of the alloy sample (black solid line) recorded together with RBS. The fit provided by the GUPIX code is also shown for comparison (red solid line).

Aiming to obtain an accurate description of the stoichiometry of the metallic elements present in the alloy with high accuracy, the GUPIX code [25] was used with the integrated charge deduced from the *particles*ΔΩ* product derivate during the RBS fit. Other fit parameters, such as the absorption filter, detector efficiency and Be-window thickness have been considered for the fitting. Furthermore, in the GUPIX code, the sample structure was defined as *Layer Thickness Interaction* (LTI), where the layer thickness is provided as input (with an initial value known from RBS and further input provide from ERD and EBS, see below). Note, that even if the fit results with and without the LTI option were rather similar a difference of around ≈ 0.8 at.% in the metallic stoichiometry was observed. For calculating input for the iterative evaluation procedure, we kept this option active, as GUPIX computes self-ionization and matrix corrections more accurately. As final result from PIXE analysis, the stoichiometry of the metallic elements in the alloy are found to be Cr = 31.7 at.%, Fe = 34.1 at.% and Ni = 34.2 at.%. The statistical uncertainties involved in their quantifications are discussed in details in Sec. 3.2. Note, that the present PIXE results, as well as the above-mentioned difference dependent on the employed model are only providing relative concentrations. These values, however, are apparently obtained with high precision.

As both RBS and in particular PIXE are rather insensitive to light species, in order to obtain absolute quantification the abundance of light elements in the alloy has to be quantified by a different approach. For this aim, two additional IBA techniques were employed self-consistently with the others: ToF-ERDA and EBS. In the former we depth-profiled the amount of C present in the film and checked for the presence of other light impurities such as H (quantification limit ≈ 0.5 at.%). In the latter we depth-profile, with higher accuracy, the amount of O in the alloy.

In Fig. 4, two experimental EBS spectra (black solid line) are shown for He^+ projectile energies of 3.037 keV and 3047 keV, panels (a) and (b), respectively. The experimental EBS spectra for each energy have been evaluated using the Multi-SIMNRA code [26] Scattering cross sections are provided by *SigmaCalc* for the non-Rutherford resonant cross-sections [16, 27] as discussed in Sec. 2.3. The non-Rutherford $^{16}O(\alpha,\alpha_0)^{16}O$ resonance has a narrow shape (≈ 10 keV) at 3037 keV, thus we have modulated the helium beam by energy steps of the same width (corresponding to a distance of x nm travelled in the material). This shifting of the resonance peak allows for depth profiling the amount of O in the sample. By comparing the panels in Fig. 4, one can see a small amount of oxygen ($9.23x10^{15}$at/cm^2 ≈ 5nm) present only at the sample surface, indicating high resistivity against corrosion.

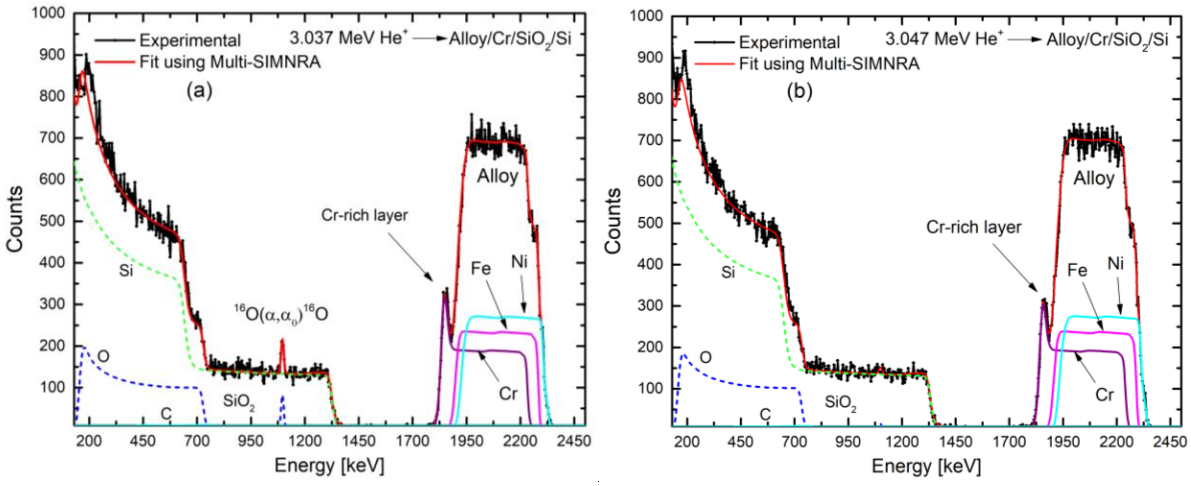

Figure 4. (Color online) Panel (a) Experimental EBS spectrum recorded at the resonance energy of 3.037 MeV, including the corresponding Multi-SIMNRA fit upon different energy spectra recorded during the EBS scan. Panel (b) same as in (a), but now the beam energy was 3.047 MeV. Oxygen was detected only on the surface of the alloy (see text for details).

In Fig. 5, the depth-profile of the constituents found in the alloy deduced from experimental ToF-ERDA spectrum is shown. The depth-profile was obtained by using the POTKU code [28], and considering the efficiencies of the ToF detectors. From this figure, a rather homogeneous depth-profile for the metallic constituents of the film (Cr, Fe and Ni) ranges from the surface until a depth of ≈ 3500 x 10^{15}at/cm^2. The total areal thickness obtained estimated by the half height of the metal signal dropping at large

depth is exceeding 4000 x 10^{15}at/cm^2 in contrast to RBS and EBS. This finding can be explained by two factors: first, the expected higher uncertainty of the inelastic energy loss of the heavy primary ion species as well as the recoils [29]. Second, at larger depth, the inevitably increasing contribution from nuclear energy losses equivalent to multiple small angle scattering events is deteriorating depth scales. Additionally, in Fig. 5 one can see depth-profiles of the other light elements (O, C and Si) present in the alloy (other colors). Considering the ToF-ERDA system and its geometry, the mass resolution for heavy and nearby elements (Cr, Fe and Ni) is relatively poor; hence, their mass signals are overlapping in the mass spectrum (not shown). Here, we summed them up and indicated as "metallic alloy" (black solid line).

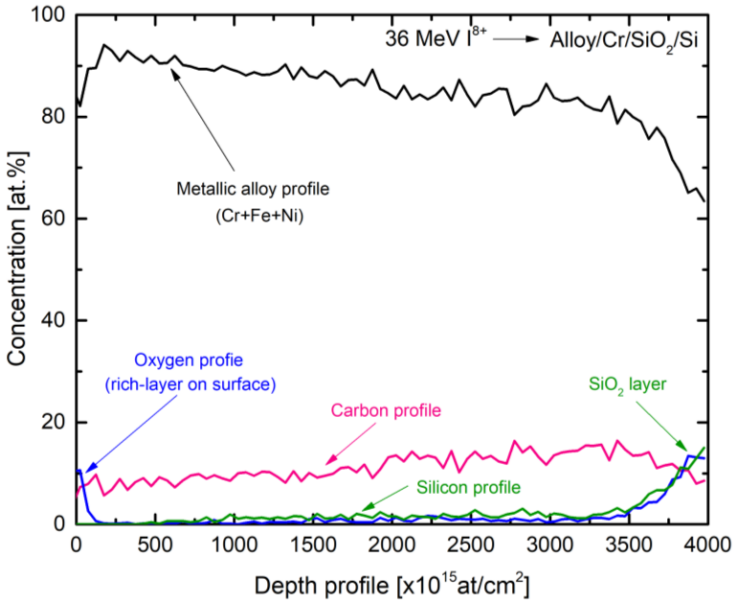

Figure 5. (Color online) Atomic concentration of the main constituents of the alloy as a function of their depth-profile deduced from the experimental ToF-ERDA spectrum using the Potku code.

According to the Fig. 5, the film features a carbon concentration of ≈ 8 at.% close to the surface, slowly increasing up to ≈ 14 at.% nearly its interface to SiO_2 layer (blue red line). Note that in ToF-ERDA, in particular for the employed heavy primary ions, the previously mentioned increasing plural and multiple scattering with decreasing energy, affects the signals. This fact, together with the associated energy loss straggling may in principle have a deteriorating effect in the obtained depth profiles, as the above mentioned effect on depth scales might differ for different recoiling species. To confirm or reject the observed gradient, a comparison with RBS is advantageous. Aiming to account for carbon in the self-consistent analysis – i.e. in the RBS and EBS fits - the carbon depth-profile was sliced into two different regions of similar thickness. In the first region [250 - 1750] x 10^{15}at/cm^2, the average carbon concentration was ≈ 9 at.%, whereas in second one, [1750 - 3250] x 10^{15}at/cm^2, a value of ≈ 12 at.% was found. These two layers with different carbon concentrations were subsequently included into the RBS and EBS fits accordingly. The effect of this addition can be seen as a slight depletion on the low-

energy signal from the alloy peak in Figs. 2 (b) and Fig. 4 improving the overall agreement with the experimental data. Thus, on the one hand the gradient can be considered as confirmed, and, in turn, the knowledge on the depth-dependent carbon profile from ToF-ERDA, although relatively small, plays a crucial role in an accurate RBS analysis (discussed above). In Fig. 5, we can also observe the presence of a thin oxygen-rich layer on surface of the film (blue solid line). Limited energy resolution and energy-loss straggling of the recoiled atoms, together with a more complex calibration of the energy-time coincidence measurements may, however, lead to poor quantification of the thickness and concentration of oxygen direct from the depth-profile shown in Fig. 5. No detectable hydrogen was found in the film, in accordance with the corrosion-resistivity expected for such metal-blends.

3.2. Budget of uncertainties

The goal of the following discussion is to perform a quantitative analysis of the main sources of uncertainties affecting our self-consistent approach. A summary of the main results deduced from different ion-beam probing techniques on the alloy thin-film, together with their associated budget of uncertainties is presented in Table 1.

Table 1. Budget of the main sources of uncertainty affecting the depth-profile obtained by employing four different IBA techniques (RBS, PIXE, EBS and ToF-ERDA). Note that the *quantity* units are shown above their values, whereas the statistical errors are all given in %.

	Oxygen-layer (surface)	*Alloy layer*					*Cr Layer*	*SiO_2 Layer*
	O [10^{15}at/cm^2]	**Cr* [%]**	**Fe* [%]**	**Ni * [%]**	**C** [%]**	**Thickness [10^{15} at/cm^2]**	**Thickness [10^{15}at/cm^2]**	**SiO_2 [µm]**
*Quantity **[units above]***	9.23	28.3	30.7	30.8	10.2	3574	120	1.2
Counting statistics [%]	4.3	1.7	2.3	3.1	1.9	0.59	2.5	<< 1
Fitting accuracy [%]	0.25	2.0	2.7	3.8	0.20	0.15	2.5	4.7
Background contribution [%]	2.1	---	---	---	1.0	<< 1	3.1	3.1
*Total STATISTICAL uncertainty **in [%]***	4.8	2.6	3.5	4.9	2.2	0.61	4.7	5.7
Main IBA technique	EBS	PIXE	PIXE	PIXE	ToF-ERDA	RBS+EBS	RBS+EBS	EBS

** Normalized with C to 100% in the layer (see text for details).*
*** Average over two different depth-integrated regions (see text for details).*

As it can be seen in Table 1, the dominant source of uncertainty comes from the statistical counts of the spectra, which can be in principle improved by longer measurement time. However, we aimed to acquire all the spectra in a regime of low current to further reduce pile-up contributions, which is almost negligible for all the analysis. Contributions from plural and multiple scattering due to the backscattered particles in the heavy-elements in the metallic alloy were considered in the fits as well and belong to the background contribution category. For instance, the oxygen resonant peak is located below the heavy-element peaks (see Fig. 4, panel a), and it sits onto the Si-background, which means the uncertainty in the Si background enters the oxygen quantification accuracy. The fitting accuracy

shown in Tab. 1 is an estimation of errors related to the physical models as well as the accuracy of different algorithms used to minimize the chi^2 implemented in the different IBA codes (SIMNRA, Multi-SIMNRA, GUPIX and Potku).

Although not shown in Tab. 1, our results are also subject to systematic uncertainties. For RBS and EBS analysis, the major systematic uncertainties are related to the *(particle*ΔΩ)* product [30] as obtained by fitting the signal of the substrate, due to two different causes: possible inaccuracies in the stopping power and residual channeling effects. Recent energy loss studies have demonstrated that either fully theoretical or semi-empirical stopping power models are expected to agree to experimental data within ≈ 1 % for H^+ and He^+ projectiles at energies ≥ 1.0 MeV [31, 32]. Nevertheless, in some particular cases, even the most recent tabulated stopping power values for light projectiles, as well as SRIM predictions, are found to be problematics, especially for reactive transition metals (such as vanadium) [33].

In this work, to fit the product particles times detector solid angle (i.e., *particles*ΔΩ)* we used an energy region in RBS and EBS spectra above 1.5 MeV, corresponding to the backscattered particles from the SiO_2 layer. The stopping power at this energy is expected to be more accurate than the statistical uncertainties shown in Table 1; hence, we did not consider it in the budget of uncertainties. Besides our efforts to "randomize" the α-backscattering yield by rotating the sample, residual channeling should be discussed as a potential source of uncertainties (see for instance discussions in Ref. [34]). Since we, however, applied the same rotation procedure whenever recording any RBS or EBS spectrum, and were able to fit all spectra self-consistently, the impact of any residual channelings in a spectrum onto accuracy of the *particles*ΔΩ* is rather small than the statistical errors in shown in Table 1.

For the PIXE analysis, systematic sources of uncertainty *a priori* would be worse. Inaccurate *particles*ΔΩ* values, eventual discrepancies on detector solid angle and perhaps problems with the internal GUPIX databases for x-ray production and absorption and matrix corrections, would lead in principle to higher systematic uncertainties. However, note that only a relative concentration of Cr-Fe-Ni in the sample was fitted by GUPIX, hence systematic errors is rather canceled out during the fit. For the ToF-ERDA, systematic uncertainties related to unknown energy loss of the recoiled atoms, connected to inefficiencies of the ToF detectors (worsening as lighter as the recoil atom is) are expected to be ≈ 5 – 10 % in absolute concentration in a stand-alone ToF-ERDA analysis.

4. Conclusions

In this work, a high-resolution depth profiling study using different ion beam analytical techniques in an iterative and self-consistent approach to characterize a co-sputtered carbon-containing alloy thin film on silicon dioxide has been performed. The employed thin film system was chosen as a representative challenging system for such quantitative analysis as it can be considered as a model system for the emerging class of multi-functional high entropy-material.

A qualitative and quantitative comparison of stand-alone analysis using the individual methods with the iterative approach has been performed. It was shown that only a combined approach using RBS together with PIXE, EBS and ToF-E ERDA yielded the total areal thickness of the alloy with inaccuracies of e.g. up to 7 % for RBS and beyond 10% for an ERD stand-alone analysis being observed. When determining stoichiometry the relative concentrations of the metal constituents Cr, Fe and Ni could be obtained with a higher precision, as in RBS and ERD, using PIXE exclusively. The final accurate concentrations with improved precision required input in form of the matrix composition and thickness from both RBS and ERD. The later indicated weak gradient of carbon in the alloy, ranging from ≈ 8 .at% close to the surface, up to ≈ 14 at.% nearby to the SiO_2 layer. Combination with RBS could confirm the existence of this gradient as well as its relevance when, in turn, improving the RBS-fitting. Finally, the oxygen content present in the alloy, with a particular focus on the surface was investigated by adopting the $^{16}O(\alpha, \alpha_0)^{16}O$ elastic reaction at 3.037 MeV to scan the bulk of the film. In comparison to ERD, which also yields information surface oxygen this method shows superior depth resolution close to the surface and more straightforward quantification independent from calibration.

The combination of several IBA techniques in an iterative and self-consistent analysis has proven to enhance the accuracy of the information that can be obtained from each independent measurement . In the present case, five different IBA spectra were analyzed simultaneously, yielding a remaining systematic uncertainty of the final description of the multi-layered sample in terms of its chemical composition depth-profile and thickness well below the average statistical accuracy, which is found better than 4%.

Acknowledgments

Support by the Carl Tryggers foundation in form of a Postdoc scholarship. Radek Holeňák acknowledges financial support from the European Union program for education Erasmus. This study was performed in the framework of the competence center FunMat-II that is financially supported by Vinnova (grant no 2016-05156). Support by VR-RFI (contracts #821-2012-5144 & #2017-00646_9) and the Swedish Foundation for Strategic Research (SSF, contract RIF14-0053) supporting accelerator operation is gratefully acknowledged.

References

[1] J. R. Tesmer and M. Nastasi, *Handbook of Modern Ion Beam Materials Analysis*, 1st ed. (Materials Research Society, Warrendale, 1995).

[2] W. K. Chu, J. M. Mayer, and M. A. Nicolet, *Backscattering spectrometry*, 1st ed. (Academic Press INC, San Diego, 1978).

[3] C.D.Lokhande, A. Ennaoui, P. S. Patil, M. Giersig, K. Diesner, M. Muller and H. Tributsch, *Chemical bath deposition of indium sulphide thin films: preparation and characterization*, Thin Solid Films **1-2** (1999) 18-23.

[4] E. Guziewicz, R. Ratajczak, M. Stachowicz, D. Snigurenko, T. A. Krajewski, C. Mieszczynski, K. Mazur, B. S. Witkowski, P. Dluzewski, K. Morawiec and A. Turos, *Atomic layer deposited ZnO films implanted with Yb: The influence of Yb location on optical and electrical properties*, Thin Solid Films **643** (2017) 7-15.

[5] C. Jeynes and J. Colaux, *Thin film depth profiling by ion beam analysis*, Analyst **141** (2016) 5944-5985

[6]J. R. Tesmer, C. J. Maggiore, M. Nastasi, J. C. Barbour and J. W. Mayer (eds.), *High energy and heavy ion beams in material analysis*, (Materials Research Society, Pittsburg, 1990).

[7] Hui-Ying Qu, D. Primetzhofer, M. A. Arvizu, Z. Qiu, U. Cindemir, C. G. Granqvist and Gunnar A. Niklasson, *Electrochemical Rejuvenation of Anodically Coloring Electrochromic Nickel Oxide Thin Films*, ACS Appl. Mater. Interfaces **9** (2017) 42420-42424.

[8] J. Jokinen, P. Haussalo, J. Keinonen, M. Ritala, D.Riihelä and M. Leskelä, *Analysis of AlN thin films by combining TOF-ERDA and NRB techniques*, Thin Solid Films **289** (1996) 159-165.

[9] R. A. Jarjis, *Nuclear cross section data for surface analysis*, Department of Physics, University of Manchester (1979).

[10] S. A. E. Johansson and J. L. Campbell, *PIXE: A novel technique for elemental analysis*, 1st ed. (John Wiley & Sons, New York 1988).

[11] J. N. Keuler, L. Lorenzen, R. D. Sanderson, V. Prozesky and W. J. Przybylowicz, *Characterization of electroless plated palladium–silver alloy membrane*, Thin Solid Films **347** (1999) 91-98.

[12] D. B. Miracle, O. N. Senkov, A critical review of high entropy alloys and related concepts, Acta Materiala **122** (2017) 448-511.

[13] J. W. Yeh, S. K. Chen, S. J. Lin, J. Y. Gan, T. S. Chin, T. T. Shun, C. H. Tsau and S. Y. Chang, Nanostructured high-entropy alloys with multiple principal elements: novel alloy design concepts and outcomes, Adv. Engineering Mat. **6** (2004) 299-303.

[14] Y. F. Ye, Q. Wang, J. Lu, C. T. Liu and Y. Yang, High-entropy alloy: challenges and prospects, Materials Today **19** (2015) 349-362.

[15] H. J. Whitlow, G. Possnert and C. S. Petersson, Quantitative mass and energy dispersive elastic recoil spectrometry: resolution and efficiency considerations, Nucl. Instrum. Meth. B **27** (1987) 448-457.

[16] J. A. Leavitt, L. C. McIntyre Jr., M. D. Ashbaugh, J. G. Oder, Z. Lin and B. Dezfouly-Arjomandy, Cross sections for 170.5 backscattering of 4He from oxygen for 4He energies between 1.8 and 5.0 MeV, Nucl. Instrum. Meth. B 44 (199) 260-265.

[17] A. F. Gurbich, *Evaluated differential cross-sections for IBA*, Nucl. Instrum. Meth. B **268** (2010) 1703-1710.

[18] J. L. Colaux, G. Terwagne and C. Jeynes, *On the traceably accurate voltage calibration of electrostatic accelerators*, Nucl. Instrum. Meth. B **349** (2015) 173-183.

[19] V. Paneta, M. Kokkoris, A. Lagoyannis, and K. Preketes-Sigalas, *Accurate accelerator energy calibration using selected resonances in proton elastic scattering and in (p,c) and (p,p0c) reactions*, Nucl. Instrum. Meth. B **406**, (2017) 108-111.

[20] P. Ström, P. Petersson, M. Rubel, and G. Possnert, *A combined segmented anode gas ionization chamber and time-of-flight detector for heavy ion elastic recoil detection analysis*, Rev. Sci. Instrum. **87** (2016) 103303-103308.

[21] Y. Zhang, H.J. Whitlow, T. Winzell, I.F. Bubb, T. Sajavaara, K. Arstila and J. Keinonen, *Detection efficiency of time-of-flight energy elastic recoil detection analysis systems*, Nucl. Instrum. Methods B **149** (1999) 477–489.

[22] M. Mayer, W. Eckstein, H. Langhuth, F. Schiettekatte, and U. V. Toussaint, *Computer simulation of ion beam analysis: Possibilities and limitations*, Nucl. Instrum. Meth. B **269**, (2011) 3006-3013.

[23] J. F. Ziegler, *SRIM The stopping and range of ions in matter*. Available at http://www.srim.org/. Accessed on July 2018.

[24] T. F. Silva, M. V .Moro, G. F. Trindade, N. Added, M. H. Tabacniks, R. J. Santos, P. L. Santana and J. R. R. Bortoleto, *Ion Beam Analysis of a-C:H films on alloy steel substrate*, Thin Solid Films **545** (2013) 171-175.

[25] J. L. Campbell, N. I. Boyd, N. Grassi, P. Bonnick and J. A. Maxwell, *The Guelph PIXE software package IV*, Nucl. Instrum. Meth. B **268** (2010) 3356-3363.

[26] T. F. Silva, C. L. Rodrigues, M. Mayer, M. V. Moro, G. F. Trindade,F. R. Aguirre, N. Added, M. A. Rizzutto and M. H. Tabacniks, *MultiSIMNRA: A computational tool for self-consistent ion beam analysis using SIMNRA*, Nucl. Instrum. Meth. B **371** (2016) 86-89.

[27] D. Abriola, N. P. Barradas, I. Bogdanovic-Radovic, M. Chiari, A. F. Gurbich, C. Jeynes, M. Kokkoris, M. Mayer, A. R. Ramos, L. Shi, I. Vickridge, *Development of a reference database for Ion Beam Analysis and future perspectives*, Nucl. Instrum. Meth. B **269** (2011) 2972-2978.

[28] K. Arstila,J. Julin, M. I. Laitinen, J. Aalto, T. Konu, S. Kärkkäinen, S. Rahkonen, M. Raunio, J. Itkonen, J. -P. Santanen, T. Tuovinen, T. Sajavaara, *Potku - New analysis software for heavy ion elastic recoil detection analysis*, Nucl. Instrum. Meth. B **331** (2014) 34-41.

[29] K. Kantre, V. Paneta and D. Primetzhofer, *Investigation of the energy loss of I in Au at energies below the Bragg peak*, Nucl. Instrum. Meth. B (article in press) (2018).

[30] J. L. Colaux and C. Jeynes, High accuracy traceable Rutherford backscaterring spectrometry of ion implanted samples, Analytical Methods 6 (2014) 120-129.

[31] H. Paul and D. Sánchez-Parcerisa, *A critical overview of recent stopping power programs for positive ions in solid elements,* Nucl. Instrum. Meth. B **312** (2013) 110-117.

[32] M. V. Moro, T. F. Silva, A. Mangiarotti, Z. O. Guimarães-Filho, M. A. Rizzutto, N. Added and M. H. Tabacniks, *Traceable stopping cross sections of Al and Mo elemental targets for 0.9-3.6 MeV protons,* Phys. Rev. A **93** (2016) 022704-022721.

[33] M. V. Moro, B. Bruckner, P. L. Grande, M. H. Tabacniks, P. Bauer and D. Primetzhofer, *Stopping cross section of vanadium for H+ and He+ ions in a large energy interval deduced from backscattering spectra,* Nucl. Instrum. Meth. B **424** (2018) 43-51.

[34] G. Lulli, E. Albertazzi, M. Bianconi, G. G. Bentini, R. Nipoti and R. Lotti, *Determination of He electronic energy loss in crystalline Si by Monte-Carlo simulation of Rutherford backscattering-channeling spectra*, Nucl. Instrum. Meth. B **170** (2000) 1-9.